

---

# BATF2 is a glutamine-responsive tumour suppressor required for type-I interferon-dependent anti-tumour immunity

---

---

Received: 6 December 2024

---

Accepted: 16 December 2025

---

Cite this article as: Gong, W., Taner, H.F., Wu, Y. *et al.* BATF2 is a glutamine-responsive tumour suppressor required for type-I interferon-dependent anti-tumour immunity. *Nat Commun* (2025). <https://doi.org/10.1038/s41467-025-68027-2>

Wang Gong, Hülya F. Taner, Yuesong Wu, Yumin He, Xingwu Zhou, Zaiye Li, Xin Hu, Charisse Ursin, Kala Chand Debnath, Kohei Okuyama, Qiang Hu, Christopher R. Donnelly, Felipe Nör, Chamila D. Perera, Emily Bellile, Arash Yunesi, Zhiqian Zhai, Mei Zhao, Wanqing Cheng, Zackary R. Fitzsimonds, Luke Broses, Jiaqian Li, Shadmehr Demehri, Deepak Nagrath, Gregory T. Wolf, Andrew G. Sikora, Yanbao Yu, Haitao Wen, Lei Wei, Steven B. Chinn, Jeffrey N. Myers, Shizuo Akira, Yuying Xie, James J. Moon & Yu Leo Lei

---

We are providing an unedited version of this manuscript to give early access to its findings. Before final publication, the manuscript will undergo further editing. Please note there may be errors present which affect the content, and all legal disclaimers apply.

If this paper is publishing under a Transparent Peer Review model then Peer Review reports will publish with the final article.

BATF2 is a glutamine-responsive tumour suppressor required for type-I interferon-dependent anti-tumour immunity

Wang Gong<sup>1,2</sup>, Hülya F. Taner<sup>3</sup>, Yuesong Wu<sup>4</sup>, Yumin He<sup>2</sup>, Xingwu Zhou<sup>5</sup>, Zaiye Li<sup>2</sup>, Xin Hu<sup>2</sup>, Charisse Ursin<sup>2</sup>, Kala Chand Debnath<sup>2</sup>, Kohei Okuyama<sup>2</sup>, Qiang Hu<sup>6</sup>, Christopher R. Donnelly<sup>7</sup>, Felipe Nör<sup>8</sup>, Chamila D. Perera<sup>9</sup>, Emily Bellile<sup>9</sup>, Arash Yunesi<sup>2,4</sup>, Zhiqian Zhai<sup>10</sup>, Mei Zhao<sup>1</sup>, Wanqing Cheng<sup>2,11</sup>, Zackary R. Fitzsimonds<sup>2</sup>, Luke Broses<sup>8</sup>, Jiaqian Li<sup>8</sup>, Shadmehr Demehri<sup>12</sup>, Deepak Nagrath<sup>13</sup>, Gregory T. Wolf<sup>14</sup>, Andrew G. Sikora<sup>1</sup>, Yanbao Yu<sup>15</sup>, Haitao Wen<sup>16</sup>, Lei Wei<sup>6</sup>, Steven B. Chinn<sup>17</sup>, Jeffrey N. Myers<sup>1</sup>, Shizuo Akira<sup>18</sup>, Yuying Xie<sup>4,19</sup>, James J. Moon<sup>3,5,13</sup>, Yu Leo Lei<sup>1,2,3,11,20,\*</sup>

<sup>1</sup> Department of Head and Neck Surgery, the University of Texas M.D. Anderson Cancer Center, Houston, TX 77030, USA.

<sup>2</sup> Department of Cancer Biology, the University of Texas M.D. Anderson Cancer Center, Houston, TX 77054, USA.

<sup>3</sup> Graduate Program in Oral Health Sciences, University of Michigan School of Dentistry, Ann Arbor, MI 48105, USA

<sup>4</sup> Department of Statistics and Probability, Michigan State University, East Lansing, MI 48824, USA

<sup>5</sup> Department of Pharmaceutical Sciences, the University of Michigan College of Pharmacy, Ann Arbor, MI 48109, USA

<sup>6</sup> Department of Biostatistics & Bioinformatics, Roswell Park Comprehensive Cancer Center, Buffalo, NY 14263, USA

<sup>7</sup> Department of Anesthesiology, Center for Translational Pain Medicine, Duke University, Durham, NC 27710, USA

<sup>8</sup> Department of Periodontics and Oral Medicine, the University of Michigan, Ann Arbor, MI 48105, USA

<sup>9</sup> The Center for Cancer Biostatistics, the University of Michigan School of Public Health, Ann Arbor, MI 48109, USA

<sup>10</sup> Department of Statistics and Data Science, University of California Los Angeles, Los Angeles, CA 90095, USA

<sup>11</sup> Graduate School of Biomedical Sciences, the University of Texas M.D. Anderson Cancer Center and UTHealth Houston, Houston, TX 77030, USA

<sup>12</sup> Center for Cancer Immunology and Cutaneous Biology Research Center, Department of Dermatology and Krantz Family Center for Cancer Research, Massachusetts General Hospital and Harvard Medical School, Boston, MA 02114, USA

<sup>13</sup> Department of Biomedical Engineering, the University of Michigan, Ann Arbor, MI 48109, USA

<sup>14</sup> Department of Otolaryngology-Head and Neck Surgery, University of Michigan Health System, Ann Arbor, Michigan, USA.

<sup>15</sup> Department of Chemistry & Biochemistry, the University of Delaware, Newark, Delaware, USA

<sup>16</sup> Department of Microbial Infection and Immunity, Ohio State University, Columbus, OH 43210, USA

<sup>17</sup> Department of Otolaryngology, the University of Pittsburgh Medical Center, Pittsburgh, PA 15213, USA

<sup>18</sup> Laboratory of Host Defense, Immunology Frontier Research Center (WPI-IFReC), Center for Advanced Modalities and DDS, Osaka University, Suita, Japan

<sup>19</sup> Department of Computational Mathematics, Science, and Engineering, Michigan State University, East Lansing, MI 48824, USA

<sup>20</sup> Department of Translational Molecular Pathology, the University of Texas M.D. Anderson Cancer Center, Houston, TX 77030, USA

\* To whom correspondence should be addressed

Address: 1901 East Road, Unit 1906, Houston, TX 77054, USA

Phone: 346-725-7121

FAX: 713-792-9636

Email: [YLeoLei@mdanderson.org](mailto:YLeoLei@mdanderson.org)

## Abstract

Recent evidence highlights the significance of a new type of tumour suppressors, which are not frequently mutated but inhibited by metabolic cues in cancers. Here, we identify BATF2 as a tumour suppressor whose expression is epigenetically silenced by glutamine in Head and Neck Squamous Cell Carcinomas (HNSCC). *BATF2* correlates with type-I interferon and Th1 signatures in human HNSCC, with correlation coefficients even stronger than those of the positive control, *STING*. The phosphorylation of BATF2 at serine 227 promotes the oligomerization of STING. *BATF2* deficiency or high glutamine levels result in higher oxygen consumption rates and metabolic profiles unfavorable for type-I interferon production. An isocaloric glutamine-rich diet abolishes STING-mediated effector cell expansion in tumours, weakening STING agonist-induced tumour control. Cancer cell-specific BATF2 expression promotes an Id2-centered T-cell effector signature, reduces T-cell exhaustion, and triggers spontaneous HNSCC rejection in a type-I interferon-dependent fashion. Utilizing syngeneic subcutaneous, orthotopic, and 24-week-long cigarette smoke carcinogen-induced HNSCC models, we demonstrate that host *Batf2* deficiency results in increased infiltration of CD206<sup>+</sup> myeloid cells and reduced effector CD8<sup>+</sup> T-cells, accelerating the initiation of cancers. Overall, we reveal a tumour suppressor *BATF2* whose loss is mediated by unique metabolic cues in the TME and drives cancer immune escape.

## Introduction

The clinical success of immune checkpoint inhibitors (ICI) proves that cancers can be separated from the normal tissue in which they arise by the immune system. The tumour mutational burden has been extensively characterized to test the hypothesis that the number of tumour-specific antigens underpins the immunogenicity of cancers. Recognizing the evidence substantiating this theory in several cancer types, some cancers with modest responses to ICI, however, harbor high mutational loads<sup>1</sup>. To understand the mechanism governing the immunogenicity of these cancers, we employed head and neck squamous cell carcinoma (HNSCC) as a model. Two distinct sets of etiological factors drive HNSCC initiation and both subsets contain high and similar levels of mutational burdens<sup>2</sup>. The human papillomavirus (HPV)-negative HNSCC is associated with cigarette smoke and heavy alcohol consumption. The HPV<sup>+</sup> HNSCC often occurs in the Waldeyer's ring where lymphoid structures are enriched. Gleaning evidence from two large cohorts of patients with HNSCC, we found that the Stimulator of Interferon Genes (STING)-type-I interferon (IFN-I) pathway underpins the immunogenicity of HNSCC. Oncogenes, high-risk HPV, and metabolic conditions can all dampen STING response<sup>3, 4, 5</sup>. Recent structural evidence shows that STING functions by assembling into large multimeric protein complexes<sup>6</sup>. Despite the clear delineation of the canonical STING-TANK Binding Kinase 1 (TBK1)-Interferon Regulatory Factor 3 (IRF3) signaling axis, key components in the STING complex contributing to cancer immune surveillance remain to be discovered.

Here, we show that Basic Leucine Zipper ATF-Like Transcription Factor 2 (BATF2) functions as a tumour suppressor by sustaining the fitness of STING. BATF2 is indispensable for the activation of the STING pathway and not required for cytoplasmic dsRNA-mediated IFN-I activation. BATF2 translocates to endoplasmic reticulum (ER)-associated membranes upon

STING stimulation and interacts with STING. We identify Serine 227 as a critical site for phosphorylation during BATF2 activation. High glutamine levels suppress the expression of BATF2 epigenetically and elevate oxidative phosphorylation to dampen IFN-I responses. BATF2 expression leads to IFN-I and  $\gamma\delta$  T-cell-dependent HNSCC rejection. A deficiency in *BATF2* results in the expedited onset of cigarette smoke carcinogen-induced HNSCC with infiltration of increased M2-like macrophages and decreased Th1 effector cells. Using human HNSCC specimens, we show that high levels of BATF2 correlate with increased CD8 $^{+}$  T-cell infiltration and that glutamine metabolism is inversely correlated with BATF2-IFN-I signatures.

## Results

### **BATF2 positively correlates with an IFN-I<sup>high</sup> and effector T-cell<sup>high</sup> signature in patients with HNSCC**

HNSCC frequently dampens the production of IFN-I through distinct mechanisms. To identify central pathways that determine HNSCC immunogenicity, we analyzed a single-cell RNA-Seq data set of human HNSCC tumour-infiltrating immune cells (PRJNA579178). After filtering out low-quality cells, we integrated 38,862 transcriptomes from HPV $^{-}$  HNSCC and 20,703 transcriptomes from HPV $^{+}$  HNSCC. To stabilize immune cell lineage segregation, we included ~70 additional marker genes in addition to the top 3,000 most differentially expressed genes to identify immune populations, as we recently reported<sup>7,8</sup>. We identified a total of 25 clusters and eight of them were significantly different from HPV $^{-}$  and HPV $^{+}$  tumour microenvironment (TME). We developed a robust visualization tool for single-cell data sets, supervised capacity preserving mapping (supCPM), which is adept at preserving the global geometry and correlating biological distance with geographic distance<sup>8,9</sup>. We rendered the structure of cellular subsets in human HNSCC using supCPM (Fig. 1a). Clusters 10, 19, and 20

were characterized by myeloid cells expressing high levels of *CXCL10*, *ISG15*, and *CD80*. Notably, these clusters were also distinguished by the cells expressing high levels of *BATF2* (Supplementary Fig. 1b). HPV<sup>+</sup> TME contained fewer  $\gamma\delta$  T-cells (cluster 4), *Batf3*<sup>+</sup> conventional dendritic cells type 1 (cDC1) (cluster 25), fewer mast cells (cluster 22), and fewer M1-like macrophages (clusters 10, 19, and 20) (Fig. 1a and Supplementary Fig. 1a). Because cells in clusters 10, 19, and 20 expressed high levels of IFN-I signatures, we next assessed the correlation between *BATF2* and IFN-I target genes in the TME. We analyzed 520 HNSCC specimens in the TCGA database and found that the levels of *BATF2* were significantly positively correlated with those of *IFNB1* ( $\rho=0.28$ , \*\*\*\*p<0.0001) and IFN target genes, including *MX1* ( $\rho=0.66$ , \*\*\*\*p<0.0001), *ISG54* ( $\rho=0.66$ , \*\*\*\*p<0.0001), *ISG15* ( $\rho=0.63$ , \*\*\*\*p<0.0001), *PD-L1* ( $\rho=0.54$ , \*\*\*\*p<0.0001), and *TNF* ( $\rho=0.23$ , p<0.0001) (Fig. 1b and Supplementary Fig. 1c). Notably, the Spearman coefficients noted in these correlations were even stronger than those for *STING* in the same data set<sup>4</sup>. We deconvolved the immune subsets in this data set using a robust cellular deconvolution tool, FARDEEP<sup>10</sup>. We found that the expression levels of *BATF2* were significantly positively correlated with the abundance of CD8<sup>+</sup> T-cells ( $\rho=0.39$ , \*\*\*\*p<0.0001), CD4<sup>+</sup> memory T-cells ( $\rho=0.53$ , \*\*\*\*p<0.0001),  $\gamma\delta$  T-cells ( $\rho=0.29$ , \*\*\*\*p<0.0001), and M1-like macrophages ( $\rho=0.38$ , \*\*\*\*p<0.0001). The expression levels of *BATF2* were significantly negatively correlated with the abundance of regulatory T-cells ( $\rho=-0.27$ , \*\*\*\*p<0.0001) (Fig. 1c and Supplementary Fig. 1d).

To validate the key findings, we stained a human HNSCC tissue microarray (TMA) consisting of 677 cores from 258 patients with a median follow-up of 60.1 months. After removing suboptimal cores, we had cores from 200 patients whose demographic characteristics are summarized (Supplementary Data 1). *BATF2* showed a broad range of staining intensity in

tumour cells and stroma. HNSCC-specific and TME-specific BATF2 staining scores were both positively correlated with CD8 scores (Fig. 1d-e). Next, we analyzed five TCGA data sets, including HNSCC ( $n = 522$ ,  $*p=0.034$ ), high-grade serous carcinoma (OV,  $n = 303$ ,  $*p=0.0181$ ), sarcoma (SARC,  $n = 260$ ,  $*p=0.0208$ ), skin cutaneous melanoma (SKCM,  $n = 471$ ,  $**p=0.00106$ ), and stomach adenocarcinoma (STAD,  $n = 415$ ,  $*p=0.0428$ ), and found that higher expression levels of BATF2 were positively correlated with patient outcomes (Supplementary Fig. 1e-i). To assess the role of BATF2 in suppressing tumour initiation, we next analyzed a group of patients with oral potentially malignant disorders (OPMD) specimens with confirmed malignant transformation (Supplementary Data 2). We performed BATF2 staining on the paired longitudinal specimens and found that BATF2 expression levels were lower in paired HNSCC than in OPMD (Fig. 1f-g). Next, to directly assess whether the expression levels of BATF2 in fresh HNSCC regulate their response to IFN agonists, we analyzed fresh human HNSCC from eight patients. We trisected the tissue into three pieces of comparable size. The first piece was injected with PBS ex vivo, the second piece was injected with 5.0  $\mu$ g CDA, and the third piece was formalin fixed and integrated into a tissue microarray (Fig. 1h). We performed qPCR using tissue homogenates and normalized the levels of *IFNB1* by *PTPRC*, the latter of which encodes CD45. We quantified BATF2 staining using ImageJ and generated BATF2 scores. Then, we performed a Spearman correlation analysis between BATF2 scores and normalized *IFNB1* expression and identified a strong positive correlation with a  $\rho$ -value of 0.86 ( $**p<0.01$ ) (Fig. 1i). The HNSCC TCGA data set does not have responder status for immunotherapy. Thus, we next examined four data sets that contained responder status to anti-PD1<sup>11</sup>. We found that the responders among patients with STAD ( $****p<0.0001$ ), SKCM ( $****p<0.0001$ ), bladder squamous cell carcinoma (BLCA,  $*p=0.02$ ), or non-small cell lung cancer (NSCLC,

\*\*\*\*p<0.0001) showed significantly higher levels of BATF2 expression than non-responders (Supplementary Fig. 1j-m). Overall, these data show that BATF2 inhibits the initiation of HNSCC and promotes anti-tumour immunity in human specimens.

### **BATF2 controls cytoplasmic DNA-mediated IFN-I response in macrophages.**

Because of the strong correlation between BATF2 and IFN-I signatures in the TME of HNSCC, we generated littermate control wildtype and *Batf2*<sup>-/-</sup> mice and validated the expression of *Batf2* in bone-marrow-derived macrophages (BMDM) (Fig. 2a). We transfected the cells with a STING agonist, interferon-stimulatory DNA (ISD), or poly(I:C), which activates the cytoplasmic dsRNA-sensing mitochondrial antiviral signaling protein (MAVS) pathway. Then, we performed bulk RNA-Seq to compare the transcriptomes between wildtype and *Batf2*<sup>-/-</sup> BMDM at baseline and stimulated conditions. We found that ISD and poly(I:C) induced potent IFN-I activation, with the upregulation of 13 *Ifna* subtypes, *Ifnb1*, *Sting*, and *Tnf*. The absence of *Batf2* lead to dampened IFN-I activation in response to ISD. However, *Batf2*<sup>-/-</sup> BMDM showed comparable IFN-I production when transfected with poly(I:C) (Fig. 2b). Notably, the expression levels of *Arg1* and *Mrc1* were suppressed when IFN-I was activated. The deletion of *Batf2* resulted in elevated levels of *Arg1* and *Mrc1* at baseline and ISD-stimulated conditions. No apparent difference in the expression of *Arg1* or *Mrc1* was noted when cells were transfected with poly(I:C) (Fig. 2b). Then, we performed gene set enrichment analysis (GSEA) and identified the most significantly altered pathways between wildtype and *Batf2*<sup>-/-</sup> BMDM when stimulated with ISD. The top five enriched pathways were cytokine receptor signaling, RNA splicing, unfolded protein binding, defense response, and response to virus (Fig. 2c). To validate these findings, we performed qPCR to assess the mRNA abundance of *Ifnb1*, pan-*Ifna*, *Cxcl10* in wildtype and *Batf2*<sup>-/-</sup> BMDM treated with two STING agonists, ISD or 2'3'-Cyclic GMP-AMP

(cGAMP). We found that the deletion of *Batf2* significantly reduced the transcription of IFN-I signature genes (Fig. 2d-e). In contrast, when the wildtype and *Batf2*<sup>-/-</sup> BMDM were transfected with MAVS agonists poly(I:C) or 5'ppp-dsRNA, both stimuli induced potent IFN-I pathway activation. However, there was no difference between the wildtype and *Batf2*<sup>-/-</sup> BMDM (Fig. 2f-g).

To substantiate the findings, we performed ELISA to measure the protein concentration of Ifn- $\beta$  in the supernatant. ISD transfection resulted in about 20 ng/ml Ifn- $\beta$  release by the wildtype BMDM. ISD-induced *Batf2*<sup>-/-</sup> BMDM produced less than 10 ng/ml of Ifn- $\beta$  in the supernatant (Fig. 2h). Similarly, a defect in *Batf2* almost abrogated cGAMP-mediated Ifn- $\beta$  production (Fig. 2i). We also noted a significant yet less prominent reduction in Ifn- $\beta$  production from the *Batf2*<sup>-/-</sup> BMDM when the cells were incubated with a non-nucleotide-based STING agonist, diABZI (Fig. 2j). In contrast, *Batf2*<sup>-/-</sup> BMDM were equally competent as the wildtype control cells in producing Ifn- $\beta$  when transfected with poly(I:C) or 5'ppp-dsRNA (Fig. 2k-l). Similar results were observed when we measured the protein levels of Tnf- $\alpha$  (Supplementary Fig. 2a-e), showing the selectivity of *Batf2* in regulating IFN-I pathways. Then, we sought to characterize the signaling events downstream of *Batf2*. Transfection with ISD resulted in the phosphorylation of Tbk1, Irf3, Sting, and Stat1 as early as 4 hrs post-treatment in wildtype BMDM. *Batf2* deficiency resulted in substantial repression of these key signaling events, abrogating the phosphorylation of Irf3 (Fig. 2m). Similarly, *Batf2*<sup>-/-</sup> BMDM exhibited lower levels of phosphorylation of Tbk1, Irf3, Sting, and Stat1 when transfected with cGAMP (Fig. 2n). In contrast, no difference in signaling was noted between wildtype and *Batf2*<sup>-/-</sup> BMDM when they were challenged with MAVS agonists (Supplementary Fig. 2f-g). These findings

suggest that BATF2 selectively engages STING to maintain the optimal levels of IFN-I production.

### **BATF2 promotes STING signaling in HNSCC cells.**

Because BATF2 is highly expressed by myeloid cells and epithelial cells, we performed a screen of a panel of HNC cell lines. FaDu and UMSCC22A cells express low levels of BATF2, while UMSCC108 and UMSCC49 express high endogenous levels of BATF2 (Supplementary Fig. 3a). First, we generated empty vector (EV) control and stable BATF2-expressing FaDu cells using retroviruses. We transfected EV control or BATF2-expressing FaDu cells with STING plasmid and found that BATF2 significantly promoted the transcription of IFN-I signature genes, including *IFNB1*, *CXCL10*, *CXCL9*, and *ISG54* (Fig. 3a). This finding was also recapitulated in UMSCC22A cells (Fig. 3b). Although most HNSCC cells, including FaDu and UMSCC22A, do not show robust IFN-I activation when transfected with cGAMP<sup>4,5</sup>, we found that BATF2 could still enhance the IFN-I response (Supplementary Fig. 3b-c). During tumour initiation, when immune surveillance determines the outcomes of epithelial transformation, the proper activation of the innate immune pathways enables the maturation of antigen-presenting cells and subsequent cross-priming of T-cells. To evaluate whether BATF2 helps to launch the IFN-I pathway against epithelial malignant transformation, we expressed BATF2 in NOM9-TK normal oral keratinocytes, which directly triggered the phosphorylation of TBK1 and STING (Supplementary Fig. 3d). To substantiate the findings, we generated EV and *BATF2*-deficient UMSCC108 and UMSCC49 cells using CRISPR-Cas9 lentiviruses. In agreement, *BATF2* deficiency in UMSCC108 and UMSCC49 cells significantly reduced STING-mediated IFN-I signature gene expression (Fig. 3c-d). Then, we examined signaling alteration by immunoblotting phosphorylation of TBK1 and STING in HNSCC cells. The expression of

BATF2 substantially increased the activation markers of the STING pathway (Fig. 3e and Supplementary Fig. 3e). BATF2 was STING-inducible, and BATF2 depletion resulted in compromised STING activation in UMSCC108 and UMSCC49 cells (Fig. 3f).

### **BATF2 translocates to the endoplasmic reticulum (ER) to interact with STING**

To characterize the staining pattern of BATF2 in the TME, we performed an immunohistochemical stain of human HNSCC specimens with an anti-BATF2 antibody. Among the BATF2<sup>+</sup> HNSCC cases, BATF2 shows a perinuclear punctate staining pattern, which can be seen in proteins localized to ER or Golgi apparatus, in addition to nuclear staining (Fig. 4a). Thus, we performed a sucrose gradient to fractionate cytosol, nuclei, and ER as reported<sup>12, 13, 14</sup>. We found that STING was enriched in the ER compartment and not identified in free cytosol, as expected. BATF2 was present in the cytosol and at a lower level in the ER in the resting state. When THP-1 cells were treated with cGAMP overnight, there was a substantial translocation of BATF2 into the ER (Fig. 4b). We also identified phosphorylated TBK1 and IRF3, two central STING signaling molecules enriched in the ER fraction when the cells were treated with cGAMP. Consistent with the transcription factor function, phosphorylated IRF3 was most highly enriched in the nuclei fraction. As controls, VDAC, a mitochondrial protein was largely absent in the ER and cytosol fractions. Lamin B1 (LMNB1) is a component of the nuclear lamina and was enriched in the nuclear fraction, as expected (Fig. 4b). To visualize the localization of BATF2, we performed a confocal imaging analysis of BATF2. We co-stained HNSCC cells with STING and MitoTracker. We noticed that BATF2 colocalized with STING but not with mitochondria (Fig. 4c). This prompted us to directly assess BATF2-STING interaction using biochemical methods. We pulled down STING under stringent buffer conditions and identified a strong interaction with BATF2 in HEK-293T cells (Fig. 4d), a model cell line free of oncogenic

mutations that often interfere with the STING-IFN-I pathway. Similarly, we pulled down BATF2 and identified STING as a binding partner (Fig. 4e). Then, we performed co-immunoprecipitation in FaDu and RAW 264.7 cells and found that BATF2 interacted with STING strongly (Fig. 4f-h). To further investigate which domain of STING specifically interacts with BATF2, we deleted the N-terminus, the Ligand-Binding Domain, or the C-terminus of STING. All STING domain truncation mutants can be expressed. We immunoprecipitated BATF2 and found that only the LBD domain was required for the BATF2-STING interaction (Fig. 4i). LBD is also the domain critical for STING oligomerization<sup>15</sup>. Thus, it is likely that the BATF2-STING interaction stabilizes the STING oligomers in an LBD-dependent fashion.

To directly assess whether BATF2-mediated IFN-I activation is STING-dependent, we depleted STING in *Batf2*-expressing tumour cells (Supplementary Fig. 4a). *Batf2* significantly increased the transcription levels of *Ifnb1*, *Isg54*, and *Cxcl9* in response to transfection of 1.0 µg/mL ISD. *Sting* deficiency abrogated *Batf2*-driven IFN-I activation (Supplementary Fig. 4b-d). Similarly, *Batf2* expression directly increased the transcription levels of *Ifnb1*, *Pan-Ifna*, and *Cxcl10* in wild-type BMDM, which was abrogated in *Sting*<sup>-/-</sup> BMDM (Supplementary Fig. 4e-g). These results substantiate the BATF2-STING-IFN-I signaling pathway.

#### **Phosphorylation of BATF2 is essential for its function in supporting STING signaling.**

Because the activation of STING depends on its oligomerization into a higher-order molecular complex<sup>15</sup> and BATF2 binds to the STING LBD domain essential for oligomerization, we sought to determine whether BATF2 was involved in the STING complex formation under native conditions. We stimulated wildtype and *Batf2*<sup>-/-</sup> BMDM with ISD and performed native gel electrophoresis. We found that the STING oligomers started to form as early as 4 hours post-transfection and became prominent at the 8-hour time point. *Batf2* depletion substantially repressed

the oligomerization of STING (Fig. 4j). The oligomerization of STING promotes its phosphorylation and downstream signaling. Then, we investigated whether BATF2 was phosphorylated during STING activation. Using PhosphoSitePlus, we found that there were two predicted phosphorylation sites for Batf2 at serine 179 and serine 227 (Fig. 4k). Then, we set out to determine whether Batf2 is phosphorylated upon STING stimulation. Because there is no phosphorylation-specific antibody available for Batf2 yet, we ran a phos-tag gel to determine whether the protein was phosphorylated. THP-1 cells were incubated with cGAMP admixed with human albumin, and we found that BATF2 was indeed phosphorylated upon stimulation. IRF3 was also immunoblotted using phos-tag gel as a positive control (Fig. 4l). To determine which phosphorylation site is indispensable for Batf2's function in regulating STING, we performed a reconstitution experiment where we transfected full-length and site-specific mutant Batf2 plasmids to *Batf2*<sup>-/-</sup> BMDM. We treated wild-type and *Batf2*<sup>-/-</sup> BMDM, in the absence or presence of reconstitution, with ISD. In agreement with Fig. 2m, *Batf2* deficiency suppressed STING signaling. Reconstituting the *Batf2*<sup>-/-</sup> BMDM with wild-type Batf2 or Batf2-179A mutant, the latter of which contained a serine to alanine mutation and cannot be phosphorylated at 179S, restored STING signaling. In contrast, reconstitution with the Batf2-227A mutant failed to restore signaling, suggesting that the phosphorylation of the 227 serine residue of Batf2 is essential for its function (Fig. 4m). To confirm whether S227 is also essential for BATF2 activation in cancer cells, we expressed wild-type BATF2 and BATF2-227A mutant in the human UMSCC22A cell line. We found that the full-length BATF2 substantially enhanced cGAMP-mediated STING activation, which was abolished by mutating S227 to an alanine (Supplementary Fig. 4h).

**Glutamine inhibits the STING-IFN-I pathway by suppressing the expression of BATF2.**

By examining the TCGA data set, the loss of *BATF2* at the genetic level is uncommon. We next sought to investigate the mechanism underpinning the suppression of *BATF2* expression in the TME. First, we tested *BATF2* expression in nutrient-defined media specifically deficient for one of the essential or non-essential amino acids (Supplementary Fig. 5a). We found that deficiency in glutamine, tyrosine, valine, isoleucine, and methionine resulted in significantly elevated expression of *BATF2* (Supplementary Fig. 5a). Recent evidence suggests that glutamine is a central anaplerotic nutrient sustaining the tricarboxylic acid cycle in cancers. Inhibition of glutamine metabolism inhibits the generation of myeloid-derived suppressor cells (MDSC) and suppresses tumour growth<sup>16</sup>. Conceptually in agreement, glutaminolysis is pivotal for alternative (M2-like) activation of macrophages<sup>17</sup>. In addition to immune cells, cancer cells show an even higher ability to uptake glutamine in the tumour microenvironment<sup>18</sup>. Because the lack of IFN-I signaling in the TME leads to MDSC expansion and M2-like differentiation, we next sought to determine whether glutamine inhibits STING-mediated IFN-I activation. We cultured BMDM in glutamine-free media, media with 0.5 g/L glutamine i.e. at the concentration of regular complete media, and media with 5.0 g/L glutamine. Transfection of BMDM with cGAMP resulted in significantly increased transcription of *Batf2* and IFN-I genes. Higher levels of glutamine significantly repressed cGAMP-induced expression of *Batf2*, *Ifnb1*, and pan-*Ifna* (Fig. 5a and Supplementary Fig. 5b-c). Similarly, we transfected BMDM with ISD and found that glutamine significantly suppressed the STING-induced expression of *Batf2* and IFN-I signature genes (Fig. 5b and Supplementary Fig. 5d-g). Treatment of cGAMP-activated BMDM with a selective glutaminase inhibitor, Bis-2-(5-phenylacetamido-1,3,4-thiadiazol-2-yl)ethyl sulfide (BPTES), significantly elevated the expression levels of *Batf2*, *Ifnb1*, and pan-*Ifna* in media containing either 0.5 g/L or 5.0 g/L glutamine (Fig. 5c-d and Supplementary Fig. 5h-i). To substantiate the findings,

we measured the protein levels of Ifn- $\beta$  (Fig. 5e-f), Tnf- $\alpha$  (Supplementary Fig. 5j-k), and Cxcl10 (Supplementary Fig. 5l) in the supernatant and recapitulated the findings using qPCR. We harvested the cells and performed immunoblotting of STING signaling markers. The addition of glutamine dampened the phosphorylation of Tbk1, Sting, and Irf3 (Fig. 5g). Similarly, in THP-1 cells, we found that 0.5 g/L and 5 g/L glutamine suppressed the transcriptional expression of *BATF2* and IFN-I target genes (Supplementary Fig. 6a). At the protein level, high concentrations of glutamine not only reduced BATF2 expression but also led to decreased phosphorylation of TBK1 and IRF3, ultimately resulting in impaired IFN- $\beta$  production (Supplementary Fig. 6b-c). To confirm glutamine-mediated BATF2-IFN-I suppression also similarly occurs in cancer cells, given their high dependence on glutamine metabolism, we transfected UMSSCC49 cells with 2.0  $\mu$ g/mL ISD with or without glutamine in the culture media. In agreement, glutamine potently inhibited the expression of BATF2 and IFN-I target genes (Supplementary Fig. 6d). At protein levels, glutamine also inhibited the expression of BATF2, the phosphorylation of TBK1, and the phosphorylation of STING (Supplementary Fig. 6e). To determine whether glutamine-mediated IFN-I suppression depends on BATF2, we transfected *Batf2*<sup>-/-</sup> BMDM with ISD with or without glutamine. In contrast to wildtype BMDM, the deficiency in *Batf2* abolished glutamine-driven suppression of Ifn- $\beta$  production suggesting that glutamine inhibits IFN-I in a *Batf2*-dependent fashion (Supplementary Fig. 6f).

To understand the mechanism underpinning glutamine-mediated suppression of BATF2, we performed a chromatin immunoprecipitation (ChIP) experiment to examine glutamine-mediated epigenetic regulation of *Batf2* and IFN-I target genes in BMDM. We found that glutamine significantly increased the levels of a repressive marker, H3K27me3 on the promoters of *Batf2*, *Ifnb1*, and *Cxcl9* (Fig. 5h and Supplementary Fig. 6g). This glutamine-mediated

epigenetic regulation was specific because glutamine had no impact on the H3K4me3 marker on the promoters of *Batf2* and *Ifnb1* (Supplementary Fig. 6h).

We showed that depletion of *Batf2* increased the expression of marker genes for the alternatively activated macrophages, such as *Arg1* and *Mrc1* (Fig. 2b). STING-IFN-I signaling promotes the classical activation of macrophages, which primarily relies on aerobic glycolysis to meet the rapidly increased energy demand. In contrast, alternative activation in macrophages favors oxidative metabolism and maintains a robust glutaminolysis program. The addition of glutamine increased the basal and maximal oxygen consumption rates (OCR) at baseline and STING-induced conditions (Fig. 5i and Supplementary Fig. 7a-b). Although wild-type and *Batf2*<sup>-/-</sup> BMDM showed comparable basal and maximal OCR at baseline without immune activation, *Batf2*<sup>-/-</sup> BMDM demonstrated a significantly higher basal and maximal OCR than the wild-type cells under STING-induced conditions (Fig. 5j and Supplementary Fig. 7c-d), similar to the high glutamine culture conditions. To further evaluate the impact of glutamine upon STING activation in vivo, we employed an isocaloric diet model where we fed C57BL/6J mice with a control diet or a glutamine-rich diet. Mice in both groups showed comparable body weight throughout the experiments (Supplementary Fig. 7e). We implanted an aggressive HNSCC model, NOOC1, which shows ~91% similarity in mutational signatures to human tobacco-associated cancers and is refractory to ICB<sup>19</sup>, in mice on a control regular diet and an isocaloric, glutamine-enriched diet. NOOC1 grew even more aggressively in mice on the glutamine-rich diet at baseline (Fig. 5k). To assess whether glutamine-mediated tumour aggression depends on the suppression of *Batf2*, we implanted the same tumour model into *Batf2*<sup>-/-</sup> mice on either a regular diet or an isocaloric, glutamine-rich diet. We found that a glutamine-rich diet could no longer promote tumour growth in the absence of host expression of *Batf2* (Supplementary Fig. 7f). For mice on a regular diet,

intra-tumoural injection of STING agonists resulted in significant tumour volume reduction, as expected (Fig. 5k). However, in mice fed with a glutamine-rich diet, STING agonists failed to show any efficacy (Fig. 5k). We used a tumour volume of 500 mm<sup>3</sup> as the cutoff point to assess mouse survival. We found that mice on a glutamine-enriched diet had significantly lower survival rates compared to those on a control diet, and CDA treatment did not improve their survival. In contrast, CDA treatment extended the survival of mice on a regular diet (Supplementary Fig. 7g). Then, we assessed the impact of inhibition of glutamine metabolism on tumour response to IFN-I agonists. In the same experiment shown in Fig. 5k, we also included two additional groups that received intra-tumoural injection of CDA and a glutaminase inhibitor, JHU083. One of these groups was on a regular diet, and the other was on an isocaloric glutamine-rich diet. Interestingly, although JHU083 did not further improve the anti-tumour efficacy of CDA in the regular diet group, it significantly improved tumour control in mice on a glutamine-rich diet (Fig. 5l-m).

To determine the mechanism of glutamine-rich diet-mediated desensitization of cancer to STING stimulation, we performed scRNA-Seq to examine changes in the TME (Fig. 5n). We utilized an optimized analytical pipeline where we included additional feature genes for lineage segregation and stabilization to identify ten main clusters<sup>7, 8</sup>. In mice on a regular diet who were treated with STING agonists, we observed an increase in CXCR5<sup>+</sup> B cells (cluster 7) and T-cells (cluster 6), along with a reduction in granulocytic MDSC infiltration (clusters 3 and 8) in the TME. In contrast, when mice were fed with an isocaloric glutamine-rich diet, intra-tumoural STING stimulation failed to increase T-cell infiltration (cluster 6) but increased the expansion of granulocytic MDSC (clusters 3 and 8). In the glutamine-rich diet group, we also observed an expansion of endothelial cells (cluster 9) and basophils (cluster 10) (Fig. 5o). To assess whether glutamine suppressed *Batf2* in vivo as a mechanistic link of dampening STING-mediated anti-

tumour immunity, we examined the expression levels of *Batf2* and found that *Batf2* was most highly expressed by tumour cells (cluster 5), *Ifnb1*<sup>+</sup>*Cxcl10*<sup>+</sup> myeloid cells (cluster 1), MHC-II<sup>+</sup> myeloid cells (cluster 2) and dendritic cells (cluster 4) (Fig. 5p). Notably, glutamine significantly decreased the expression of *Batf2* in vivo (Fig. 5q). In the myeloid cell cluster that features high expression levels of *Ifnb1* and *Cxcl10*, a glutamine-rich diet significantly reduced the levels of *Batf2* and *Ifnb1* (Supplementary Fig. 7h-i). We and others have shown that STING agonists significantly expanded the infiltration of effector and stem-like T-cells<sup>5, 20, 21</sup>. Thus, we sub-clustered T-cells (cluster 6) into functional subsets to better assess the impact of a glutamine-rich diet on cancer STING response (Supplementary Fig. 7j-k). In agreement with the literature, STING agonists substantially expanded intra-tumoural CD8<sup>+</sup> T-cells (subcluster 2), NK cells (subcluster 3), and Tcf7<sup>+</sup> T-cells (subcluster 4) in mice on a regular diet. In contrast, STING agonists failed to expand these key anti-tumour immune subsets in mice on an isocaloric glutamine-rich diet (Supplementary Fig. 7j-k). As we saw a noted B-cell expansion in response to STING stimulation only among mice on a regular diet, we next examined the B-cell signatures and found that STING stimulation is more prominently promoting the upregulation of multiple functional B-cell subset markers in tumours grown in mice on a regular diet than those grown in mice on a glutamine-rich diet, including *Cr2*, *Fcer2a*, *Igkc*, *Ighm*, *Ighd*, *Sell*, *Ms4a1*, *Sdc1*, *CD79a*, *CD19*, and *Cxcr5* (Supplemental Fig. 7l). In agreement, we quantified CD20 staining of tumours from different treatment groups and found that STING stimulation expanded B-cells in the tumours grown in mice on a regular diet but not in mice on a glutamine-rich diet (Supplemental Fig. 7m). To substantiate the physiological relevance of the glutamine-BATF2 pathway, we collected fresh HNSCC tissue from 15 patients (Supplementary Data 3) and performed bulk RNA-Seq. Then, we performed a correlation analysis between BATF2-IFN-I pathway genes and glutamine metabolism

markers. We found that *BATF2* was strongly positively correlated with Th1 genes, including *CXCL9*, *CXCL10*, *ISG15*, *IFNB1*, *OASL*, and *TNF*. Notably, we also found that *BATF2* was inversely correlated with glutamine metabolism pathway genes, such as *SLC7A5*, *SLC1A5*, *SLC38A2*, and *GLS*. In agreement, the Th1 cytokines, including *IFNG*, *IFNB1*, and *TNF*, all show an inverse correlation with glutamine metabolism (Fig. 5r). Collectively, these findings suggest that high glutamine levels silence the expression of *BATF2* by increasing the trimethylation of lysine 27 on histone H3 protein, promoting a metabolic profile recalcitrant to STING stimulation.

### **HNSCC-specific BATF2 promotes IFN-I- and $\gamma\delta$ T-cell-dependent tumour immunogenicity.**

The use of a cigarette smoke carcinogen, 4-nitroquinoline 1-oxide (4-NQO), could generate tumour cells with high similarity mutational profiles to human tobacco-associated cancers, such as HNSCC<sup>19, 22</sup>. Thus, we treated C57BL/6J mice with 50 µg/mL 4-NQO-containing drinking water for 16 weeks. Then, we switched the mouse cages to regular water and monitored the development of HNSCC. A histology-verified tongue squamous cell carcinoma was processed to produce single-cell clones. Every single cell-derived line was expanded and screened in C57BL6/J mice for tumour establishment. Most clones were spontaneously rejected except for two 4-NQO-induced Oral Cancer (NOOC) lines, NOOC1 and NOOC2. Similar to NOOC1, which has a combined 91% similarity in mutational signatures to human tobacco-associated cancers, NOOC2 has a combined >95% similarity in mutational signatures to human tobacco-associated cancers, including 68.1% similarity to Single Base Substitution (SBS)4 (tobacco smoking), 18.3% similarity to SBS5 (tobacco smoking), and 13.6% similarity to SBS14 (defective DNA mismatch repair) (Supplementary Fig. 8a). Common HNSCC missense mutations, such as *Trp53* (R178P), *Erbb2* (P1034L), *Nsd1* (E1342\*), *Kmt2d* (R5157L, R3551L,

E3060K), *Kdm5c* (E1496\*), *Kdm6a* (Q475H), *Fgfr3* (G444S), *Fat1* (Q901K), *Fat1* (S1372I), and *Fat1* (V2754M), were identified in NOOC2 (Supplementary Data 4). Unlike NOOC1, which is completely refractory to high doses of ICI<sup>19</sup>, NOOC2 partially responds to a combination of anti-Pd-1 and anti-Ctla4 (Supplementary Fig. 8b).

To directly assess the role of cancer cell-specific *Batf2* expression in tumour immunogenicity, we first measured *Batf2* expression levels in MOC2-E6/E7, NOOC1, and NOOC2 cells using qPCR and found that *Batf2* expression was lowest in MOC2-E6/E7, which corresponded to the lowest transcription levels of *Ifnb1* at baseline (Supplementary Fig. 9a). Then, we generated stable *Batf2*-expressing MOC2-E6/E7 cells (Supplementary Fig. 9b). We previously showed that MOC2-E6/E7 is refractory to anti-PD-L1 and partially responsive to non-formulated CDN<sup>5</sup>. Similar to human HNSCC cells shown in Fig. 3, *Batf2* upregulated STING-induced transcription of IFN-I target genes and *Ifn-β* secretion into the supernatant (Fig. 6a-b). *Batf2* expression also increased STING-induced phosphorylation of *Tbk1*, *Irf3*, and *Sting* in MOC2-E6/E7 cells (Fig. 6c). We did not find any differences in colony formation or proliferation between the empty vector (EV) control and *Batf2*-expressing cancer cells *in vitro* (Supplementary Fig. 9c-d). However, *Batf2*-expressing tumours were spontaneously rejected in wild-type C57BL6/J mice (Fig. 6d). We extracted mRNA from homogenized tumour tissues from both groups and found that the transcription levels of IFN signature genes, including *Mx1*, *Cxcl9*, *Cxcl10*, and *Ifng* were much higher in *Batf2*-expressing tumours (Supplementary Fig. 9e). To determine whether *Batf2*-mediated tumour rejection was dependent on IFN-I, we implanted EV and *Batf2*-expressing tumour cells in *Ifnar1*<sup>-/-</sup> mice and completed rescued the phenotype (Fig. 6e). To determine whether *Batf2*-mediated tumour rejection depends on *Sting*, we generated stable empty vector control and *Sting*-deficient *Batf2*-expressing MOC2-E6/E7 cells.

We found that cancer cell-specific Batf2-mediated tumour rejection depended on cancer cell expression of Sting because knocking down *Sting* abrogated Batf2-mediated protection (Supplementary Fig. 9f-g). To discover the mechanism of cancer cell-specific Batf2 activation in tumour suppression, we characterized the temporal dynamics of the TME between control and Batf2-expressing tumours by analyzing TILs procured on days 7, 14, and 21 post-tumour implantation (Supplementary Fig. 10a). Batf2-expressing tumours demonstrated a more favorable TME at the earliest time point, as evidenced by the early expansion of CD45<sup>+</sup>CD3<sup>-</sup> CD11b<sup>+</sup> myeloid cells that are positive phospho-Tbk1 and phospho-Irf3. Also noticeable at this early time point was the expansion of  $\gamma\delta$  T-cells. Then, at the later time points, Batf2-expressing tumours started to show significantly more CD8<sup>+</sup> T-cells infiltration than control tumours, although this advantage appeared to become smaller as the tumour size continued to increase (Fig. 6f-i). These findings suggested that cancer cell-specific Batf2 expression reprograms innate and adaptive immune wiring in a stepwise fashion, with IFN-I activation in CD11b<sup>+</sup> myeloid cells and  $\gamma\delta$  T-cells expansion as the earliest response feature, followed by expansion of CD8<sup>+</sup> T-cells.

Then, we profiled the tumour-infiltrating immune cells at single-cell resolution. The significantly expanded clusters in the Batf2-expressing tumours included a subset of *Cxcl10*<sup>high</sup> myeloid cells, endothelial cells, and  $\gamma\delta$  T-cells (Fig. 6j-k). To interrogate the differences in T-cell functions, we separated T-cells (clusters 13 and 16) and identified a list of genes that were differentially expressed between T-cells from EV and Batf2-expressing tumours. The T-cells in the control TME expressed high levels of exhaustion signatures such as *Pdcd1*, *Havcr2*, and *Icos*. In contrast, the T-cells in the TME of Batf2-expressing tumours expressed significantly higher levels of *Id2* (Fig. 6l), which is indispensable for the generation of memory and effector

T-cells<sup>23</sup>. Then, we performed a gene set enrichment analysis. We found that the pathways that were significantly upregulated in T-cells from Batf2-expressing tumours included effector functions, such as Ifn- $\gamma$  response, allograft rejection, Ifn- $\alpha$  response, as well as cell proliferation, such as E2F targets, mitotic spindle, G2M checkpoint, and Myc targets (Fig. 6m). Because we observed a significant expansion of  $\gamma\delta$  T-cells in BATF2-expressing human and murine HNSCC (Fig. 1c, Fig. 6h, and Fig. 6j-k), we then investigated whether this population was essential for tumour immunogenicity. We implanted EV and Batf2-expressing tumours in *Tcrd*<sup>-/-</sup> mice and found that the lack of  $\gamma\delta$  T-cells abrogated Batf2-mediated tumour rejection, highlighting the importance of this subset in early tumour suppression (Supplementary Fig. 9h). Cxcl10 is a key target gene of Ifn- $\beta$ , and Batf2 led to a significant expansion of Cxcl10 $^{+}$  myeloid cells. Thus, we evaluated whether the anti-tumoural function of BATF2 depends on Cxcl10. We administered 200  $\mu$ g of anti-Cxcl10 neutralizing antibody on day 7 after Batf2-MOC2-E6/E7 tumour implantation, followed by 100  $\mu$ g twice per week for a total of five dosages. We found that neutralizing Cxcl10 reversed the antitumour effect of Batf2 (Supplementary Fig. 9i). Then, we sought to determine whether Batf2-mediated protection depends on  $\alpha\beta$  effector T-cells. We administered 0.5 mg of anti-CD8 antibody intraperitoneally for three consecutive days starting three days before tumour implantation, followed by twice per week injections for a total of five doses. We found that depletion of CD8 $^{+}$  T cells abrogated Batf2-mediated protection (Supplementary Fig. 9j). To determine whether cancer cell-specific Batf2 expression has an abscopal effect, we implanted the EV control and Batf2-expressing tumours on the right flank. As expected, we observed a significant reduction in tumour volume when Batf2 was expressed. However, the EV control tumours grown in the left flank of mice that bear Batf2-expressing tumours in the right flank did not show a difference in volume compared to those EV tumours

grown in the left flank of mice that bear EV tumours in the right flank (Supplementary Fig. 9k).

These data suggest that the BATF2-expressing tumour activates a local immune response without triggering a notable abscopal effect.

To further support our findings, we knocked down *Batf2* in NOOC2 cells, which have higher endogenous *Batf2* expression levels. Depletion of *Batf2* significantly reduced the production of *Ifnb1* (Supplementary Fig. 9l). In agreement, sh-*Batf2* NOOC2 tumours grew significantly faster than EV control tumours (Supplementary Fig. 9m). We demonstrated the role of the S227 phosphorylation site in *Batf2* activation. To substantiate the physiological relevance of this finding, we established tumour models that stably express empty vector, wild-type *Batf2*, and 227A mutant *Batf2*. In agreement with our other data, expression of *Batf2* inhibited tumour growth. However, *Batf2*-mediated protection was abrogated by mutating serine 227 to alanine and disabling phosphorylation at this amino acid (Supplementary Fig. 9n).

### **BATF2 expression in the host deters the initiation of HNSCC.**

To understand the impact of host BATF2 signaling on the immunogenicity of HNSCC, we first implanted MOC2-E6/E7 cells into littermate control wild-type and *Batf2*<sup>-/-</sup> mice. We observed significantly accelerated MOC2-E6/E7 tumour growth in the *Batf2*<sup>-/-</sup> host (Fig. 7a). Flow cytometric analysis of the TME showed that fewer p-Irf3<sup>+</sup>, CD4<sup>+</sup>, CD8<sup>+</sup>, and CD8<sup>+</sup>Ifn- $\gamma$ <sup>+</sup> T cells were present in tumours growing in *Batf2*<sup>-/-</sup> mice (Fig. 7b and Supplementary Fig. 10b). Similarly, we observed fewer  $\gamma\delta$  T-cells in tumours grown in the *Batf2*<sup>-/-</sup> hosts (Supplementary Fig. 11a). Using another model, we implanted NOOC2 into littermate control wild-type and *Batf2*<sup>-/-</sup> mice and consistently found that the tumour burden was significantly higher in the *Batf2*<sup>-/-</sup> mice (Fig. 7c). Consistent with previous results, host deficiency in *Batf2* resulted in fewer p-Irf3<sup>+</sup>, CD4<sup>+</sup> and CD8<sup>+</sup> T-cells infiltration in the TME (Fig. 7d). To further substantiate the

findings, we employed the third model, 4MOSC1, which only grows orthotopically in the tongue. *Batf2*<sup>-/-</sup> hosts developed the largest tongue tumours (Fig. 7e).

Implantable tumour models can provide insight into the role of cancer cell-immune cell interaction in the TME, but bypass an important phase in cancer establishment – malignant transformation. HNSCC is preceded by precursor lesions known as epithelial dysplasia. Given the critical role of IFN-I in immune surveillance, we next sought to determine whether BATF2 suppresses tumour initiation using a 22-week-long carcinogen exposure model for HNSCC. The 4-NQO-induced HNSCC follows the pathological course of epithelial dysplasia transformation. We fed wildtype and *Batf2*<sup>-/-</sup> mice with drinking water containing 50 µg/mL 4-NQO for 16 weeks and switched to regular water afterward. We found that *Batf2*<sup>-/-</sup> mice showed shorter oral lesion-free survival (Fig. 7f). We started monitoring oral lesions weekly 10 weeks post-treatment start date. The oral lesions started to appear 14 weeks post-treatment initiation. We classified tumours based on their clinical measurements and found that the *Batf2*<sup>-/-</sup> mice showed a higher disease burden (Fig. 7g and Supplementary Fig. 10b). Notably, the deficiency in *Batf2* lead to broad-field cancerization. The 4-NQO model in wild-type mice almost exclusively induces lesions in the tongue, in agreement with the literature<sup>24</sup>. We found that *Batf2*<sup>-/-</sup> mice were much more prone to developing tumours in the buccal mucosa and palate, in addition to the oral tongue (Supplementary Fig. 11c).

The 4-NQO model bears a high histologic resemblance to human HNSCC, with architectural disturbance, the transition between dysplastic epithelium and invasive tumour islands, keratin pearl formation, cytologic atypia, increased mitotic count, stromal complexity, and variably dense inflammatory cell infiltrate (Supplementary Fig. 11d). To determine whether a *Batf2* defect remodeled the infiltrating immune cell landscape, we performed spatial protein

marker analyses. We first examined the percentage of different immune subsets and found that the HNSCC in the *Batf2*<sup>-/-</sup> hosts showed significantly increased levels of CD206<sup>+</sup> macrophages, PD-L1<sup>+</sup> myeloid cells, Ly6g<sup>+</sup> MDSC, decreased levels of Tbet<sup>+</sup>CD4<sup>+</sup>, and significantly decreased expression of nuclear T-bet in CD8<sup>+</sup> T-cells (Fig. 7h-i, and Supplementary Fig. 10e-f). To map the intercellular relationships, we performed the nearest neighbor analysis and found that the distances between the following pairs of markers were significantly reduced in 4-NQO-induced HNSCC in *Batf2*<sup>-/-</sup> mice: from CD206<sup>+</sup> to CD206<sup>+</sup> cells, from PD-L1<sup>+</sup> to CD206<sup>+</sup> cells, from CD4<sup>+</sup> to CD206<sup>+</sup> cells, and from Tbet<sup>+</sup>CD4<sup>+</sup> to CD206<sup>+</sup> cells (Supplementary Fig. 11g). These findings suggest that BATF2 promotes the expansion of effector population in the TME of HNSCC.

## Discussion

Clinical evidence shows that the number of tumour-specific antigens in HNSCC does not correlate with their immunogenicity<sup>1</sup>. HNSCC are highly mutated yet only show a modest response rate to ICB. We previously found that STING is indispensable for the immunogenicity of HNSCC<sup>4</sup>. STING stimulation sensitized cancer to ICB in mouse models<sup>5, 25, 26, 27, 28, 29, 30, 31</sup>. Multiple clinical strategies, such as irradiation and DNA damage repair inhibition, converge on the STING pathway for effective immune priming. However, recent phase I trials showed that a substantial portion of patients with cancer were insensitive to STING agonists, even in combination with ICB<sup>20, 32</sup>. The data suggest that additional mechanisms dictate cancer responses to STING stimulation. Although point mutations or genetic deletion of *STING* are uncommon in squamous cell carcinomas, it is heavily targeted through four types of mechanisms. First, HNSCC oncogenes, such as *SOX2*, and HPV16 *E7*, promote the rapid turnover of STING, suppressing the downstream signaling<sup>4, 5</sup>. Second, the expression of STING is often lost through

post-transcriptional or post-translational modifications<sup>26</sup>. Third, palmitoylation is a unique modification for STING that directs it to the ER membrane<sup>33</sup>. Cancers can suppress the palmitoylation of STING by inhibiting the protein S-acyltransferases, also known as the DHHC enzymes, which are a family of enzymes responsible for attaching a palmitate molecule to cysteine residues on proteins<sup>34</sup>. Last but not least, certain metabolic conditions can serve as a rheostat for the downstream TBK1 signaling. For example, we previously found that saturated fatty acids, but not unsaturated fatty acids, potently inhibit STING, driving more aggressive HNSCC growth in obese mice<sup>3</sup>. This study identified a glutamine-inhibited tumour suppressor, BATF2, which maintains the fitness of STING-IFN-I signaling. This is conceptually in agreement that glutaminolysis underpins M2-like polarization of macrophages<sup>17</sup>. Inhibition of glutamine metabolism can reduce MDSC and improve effector T-cell infiltration<sup>16, 35</sup>. Human cancers frequently exhibit resistance to STING-inducing therapies, but the mechanism is not entirely clear. Using fresh human oral squamous cell carcinoma specimens, which showed a broad dynamic range of IFN-I production in response to STING agonists, we identified a positive correlation between BATF2 and tumour response to STING agonists. In addition, we found that BATF2 and IFN-I target genes were largely inversely correlated with glutamine metabolism genes, substantiating the physiological relevance of glutamine-mediated BATF2-IFN-I suppression.

Epigenetic control of macrophage alternative activation has been characterized in depth. The repressive mark H3K27me3 deposition on the promoters of immune suppressive *Arg1* and *Mrc1* can be reduced by IL4 through Jmjd3-dependent demethylation<sup>36</sup>. Glutamine potentiates M2-like polarization of macrophages by enabling Jmjd3-dependent reduction of H3K27me3 deposition on the promoters of *Arg1*, *Ym1*, *Retnla*, and *Mrc1*<sup>17</sup>. Conceptually in agreement, here

we show that glutamine can simultaneously promote the deposition of H3K27me3 on the promoter of *BATF2* and IFN-I target genes. Enhancer Of Zeste 2 Polycomb Repressive Complex 2 Subunit (EZH2) is a key enzyme that methylates H3K27. Recent studies show that inhibition of EZH2 potentiates IFN-I<sup>37</sup>, which supports this mechanistic link. Thus, in addition to improving the pharmacokinetic properties of STING agonists, the development of strategies to overcome *BATF2*-dependence, such as inhibition of EZH2 or glutamine metabolism, is promising to sensitize cancers to STING-mediated immune priming approaches. Indeed, we found that although inhibition of glutamine metabolism did not further strengthen low-dose, non-formulated CDN's effect on tumour control in mice on a regular diet, JHU083, a glutaminase inhibitor, sensitized tumours to STING stimulation in mice on an isocaloric glutamine-rich diet.

The classical tumour suppressor genes are defined as those whose loss at the genetic level or mutations enable early tumour onset. Here we show that *BATF2* potentially informs a class of genes with tumour-inhibitory function but are primarily regulated at epigenetic levels by the unique metabolic cues in the TME. Interestingly, glutamine is not the only metabolite that dampens *BATF2* expression. Through a comprehensive screen using defined nutrient deficiency media, we tested five non-essential amino acids and ten essential amino acids and found that only five amino acids, including glutamine, tyrosine, valine, isoleucine, and methionine, can repress *BATF2*. Conceptually in agreement with our findings of glutamine-rich diet's suppression of the STING-IFN-I pathway, dietary methionine restriction enhances STING-IFN-I activation<sup>38</sup>. We developed robust, high-fidelity NOOC1 and NOOC2 syngeneic models, in combination with carcinogen-induced models, to substantiate the tumour-inhibitory function of *BATF2* in HNSCC. However, the tumour suppressor role of *BATF2* is not limited to HNSCC. *BATF2* was shown to sensitize gastric cancer to 5-FU<sup>39</sup>. *BATF2* can promote CD8<sup>+</sup> T-cell

infiltration in patients with non-small cell lung cancer<sup>40</sup>. BATF2 is also a tumour suppressor in glioblastoma by inhibiting the recruitment of MDSC<sup>41</sup>. Here, we coined a molecular mechanism underpinning the tumour suppressor function of BATF2. BATF2 binds to the LBD of STING to facilitate STING oligomerization. The phosphorylation of BATF2 at S227 is critical for its immune-activating role. Tumours expressing wild-type BATF2 are spontaneously rejected while tumours expressing the S227A BATF2 mutant failed to be recognized by the immune system. BATF2-mediated immune recognition of cancer is potentiated by stepwise infiltration of phospho-Tbk1<sup>+</sup>, phospho-Irf3<sup>+</sup> CD11b<sup>+</sup> cells and  $\gamma\delta$  T-cells at early timepoints, followed by significant expansion of effector  $\alpha\beta$  T-cells. BATF2 is most highly expressed by epithelial cells and myeloid cells. In addition to its cancer cell-specific role, host BATF2 expression potentiates effector T-cell expansion. To mitigate BATF2 suppression, we identified glutamine metabolism in the TME as a central metabolic cue that suppresses IFN-I response in a BATF2-dependent fashion. Diet enrichment of glutamine dampens cancer response to IFN-I agonists. In agreement, pharmacological inhibitors of glutamine metabolism significantly restored IFN-I response and sensitized refractory tumours to STING agonists, especially in hosts on a glutamine-rich diet. Overall, by taking integrated analyses of human samples, molecular pathways, and pre-clinical models, we have identified BATF2 activation as a central glutamine-responsive, tumour-suppressive pathway shaping the plasticity of STING response and HNSCC immunogenicity.

## Methods

### Ethical statement

All animal experiments were conducted in accordance with institutional guidelines and approved by the Institutional Animal Care and Use Committees (IACUC) of the University of

Michigan (PRO00010232) and the University of Texas M.D. Anderson Cancer Center (00002478). The human specimen analysis was approved by Institutional Review Board (IRB) protocols HUM00113038 and HUM00042189 at the University of Michigan and 2024-0364 at the University of Texas M.D. Anderson Cancer Center.

### Cell culture and treatments

The HNSCC cell lines FaDu, UMSCC22A, UMSCC22B, UMSCC108, PCI13, and UMSCC49 were maintained in DMEM (10-013-CV, Corning) supplemented with 10% FBS (Gibco, Life Technologies) and 100 U/mL penicillin-streptomycin (15-140-122, Gibco). THP-1 cells were cultured in RPMI 1640 (MT10040CV, Corning) supplemented with 10% heat-inactivated FBS (Gibco, Life Technologies) and 100 U/mL penicillin-streptomycin (15-140-122, Gibco). HEK-293T and RAW264.7 were cultured in the same medium as HNSCC cell lines. MOC2-E6/E7, NOOC1, and NOOC2 cell lines were cultured in the 60% IMDM (SH30228.01, HyClone) with 30% F12 nutrient mix (11764-054, Gibco), 5% FBS, 5 µg/mL insulin, 40 ng/mL hydrocortisone, 5 ng/mL EGF, 100 U/mL penicillin, and 100 mg/mL streptomycin. 4MOSC1 cells were cultured as previously reported<sup>22</sup>. NOM9-TK cells were cultured in oral keratinocyte medium (ScienCell, Catalog No.#2611). The defined amino acid deficiency media were formulated as previously reported<sup>42</sup>. BMDM were isolated from both male and female littermate wild-type C57BL/6J and *Batf2*<sup>-/-</sup> mice femurs and differentiated as described earlier<sup>3</sup>. The experimental BMDM were plated in DMEM containing 20% heat-inactivated FBS and 100 U/mL penicillin/streptomycin for the indicated treatment. In the experiments evaluating the impact of glutamine on the IFN-I pathway, BMDM were seeded in a medium containing 90% glutamine-free RPMI 1640 (21870076, Gibco), 10% dialyzed FBS (SH30079.01, HyClone) and indicated levels of L-glutamine (25030081, Gibco). Cells were cultured in a 37°C humidified

incubator with 5% CO<sub>2</sub>. Treatments included 2'3'-cGAMP (tlrl-nacga23, Invivogen), ISD (tlrl-isdn, Invivogen), poly(I:C) (tlrl-pic, Invivogen), 5'ppp-dsRNA (tlrl-3prna, Invivogen), diABZI (tlrl-diabzi-2, Invivogen) and BPTES (SML0601, Sigma) as described in paper. NOOC1, NOOC2, and UMSCC cell lines were authenticated by STR profiling. FaDu, HEK-293T cells, and THP-1 cells were from ATCC. Other cell lines were not authenticated. All cell lines tested negative for mycoplasma contamination.

## Animals

We obtained six to eight-week-old C57BL/6J (strain 000664) mice from the Jackson Laboratory. The *Ifnar1*<sup>-/-</sup> strain backcrossed to the C57BL6/J background for over nine generations was reported<sup>3</sup>. The *Rag1*<sup>-/-</sup> (strain 002216) and *Sting*<sup>-/-</sup> (Strain 017537) mice were acquired from the Jackson Laboratory. The sperms of *Batf2*<sup>-/-</sup> mice were kindly provided by Dr. Shizuo Akira. The cryorecovery was performed by Taconic. The mice were genotyped by the following primers: Batf2 shextra 5'-ACATCGGTCTCAGAGAGTTGGAGTGG-3', Batf2 WT 5'-TAGGCCCTTCTCTAGAAGAAGGATGG-3', Batf2 KO 5'-CTAAAGCGCATGCTCCAGACTGCCCTG-3'. Mice were kept under specific pathogen-free conditions in a 12 h:12 h light:dark cycle with a room temperature of 72°F and an air relative humidity of 57%. For the 4-NQO-induced HNSCC mouse model, wildtype and *Batf2*<sup>-/-</sup> mice were fed with drinking water containing 50 µg/mL 4-NQO for 16 weeks before regular water feeding for an additional six weeks. We started to monitor oral lesions ten weeks post-starting date. For the glutamine diet experiments, 6-12-week-old C57BL/6J mice were provided with a diet that contained 15 kcal% fat, 200 g glutamine and 181 g carbohydrates / 3,947 kcal (A16070103, Research Diets) or a control diet that contained 15 kcal% fat and 381 g

carbohydrates / 3,947 kcal (A11112201, Research Diets) on the same day when tumour cells were implanted. Anti-mouse CD8 $\alpha$  (BE0061, Bio X Cell, Clone: 2.43), anti-mouse Cxcl10 (BE0040, Bio X Cell, Clone: 1F11), anti-Pd-1 (BP0033-2, Bio X Cell, Clone: J43) and anti-Ctla-4 antibody (BP0131, Bio X Cell, Clone: 9H10) were administered by intraperitoneal injection. Free c-di-AMP (tlrl-nacda-5, Invivogen) was administered via intra-tumoural injections or in combination with JHU-083 (HY-122218, MCE) by PO at 1.82 mg/kg when the average tumour size reached 150 mm<sup>3</sup>. Mice were humanely euthanized when the tumour volume reached 2,000 mm<sup>3</sup> or the ulceration exceeded 50% of the tumour surface area.

### **Human specimen analysis**

Human specimens were from the Oral Pathology and Head and Neck Surgery services. HNSCC specimen analysis was approved by IRB protocols HUM00113038 and HUM00042189 at the University of Michigan and 2024-0364 at the University of Texas M.D. Anderson Cancer Center. Informed consent was obtained for specimens utilized for bulk RNA-Seq. All specimens were de-identified, and the aggregated patient's demographic information is summarized in Supplementary Data 1-3. The HNSCC tissues used in this experiment have been exhausted and are unavailable. In the TMA analysis shown in Fig. 1e, the investigators were blinded to the CD8 $^+$  T-cell counts within the tumour microenvironment.

### **Gene expression and knockout**

We generated BATF2-expressing retroviruses and transduced human HNSCC cells (FaDu and UMSCC22A) and murine HNSCC cells MOC2-E6/7 with retroviruses to produce stable cell lines. We generated the BATF2-179A and BATF2-227A mutants, which contain serine-to-alanine mutations and cannot be phosphorylated at 179S and 227S by using a Site-Directed Mutagenesis Kit (E0554S, NEB). We generated *BATF2*-targeted CRISPR-Cas9

lentiviruses using a single-guide RNA (sgRNA): 5'-CACCGTGCACCTCTGTGGGGCAAT - 3'. We transduced UMSCC108 and UMSCC49 with the BATF2-targeted CRISPR/Cas9 lentiviruses and generated stable cell lines. We generated *Batf2*-targeted and *Sting*-targeted lentiviruses using shRNA (shBatf2: 5'-GCACGAATCCTGGAGAAACA-3' and shSting: 5'-CAACATTCGATTCCGAGATAT-3') and transduced them with MOC2-E6/7 or NOOC2 cells. We transduced the same cell line with empty vector lentiviruses to generate the control cells. STING domain truncation mutants were generated by PCR amplification using sequence-specific primers. The PCR product and the pcDNA3.1-Flag backbone were digested with NotI and EcoRI restriction endonucleases, gel-purified, and subsequently ligated with T4 DNA ligase. The ligation mixture was transformed into Stbl3 competent cells, and colonies were selected on LB agar containing ampicillin (100 µg/mL). After plasmid extraction, the constructs were validated by Sanger sequencing and further confirmed by Western blot analysis to ensure optimal expression.

### **Immunoblot and immunoprecipitation**

Cells were washed with 1× PBS twice and then lysed in 1× RIPA buffer (9806, Cell Signaling Technology) supplemented with an EDTA-free protease inhibitor cocktail (11836170001, Roche) and phosphatase inhibitor cocktail (78420, Thermo Fisher Scientific). The protein concentration was measured by a BCA kit (23225, Thermo Fisher Scientific) and boiled with 4× sample buffer (NP0007, Invitrogen) for 5 minutes at 95 °C. Prepared lysates were loaded on NuPAGE 4 to 12% (NP0323BOX, Thermo Fisher Scientific) or 16% (XP00162BOX, Thermo Fisher Scientific) Bis-Tris Gel. Followed by blocking in 10% milk, membrane was incubated in 5% milk with the primary antibodies: BATF2 Antibody (ab204510, Abcam, dilution 1:400), Phospho-TBK1(Ser172) Antibody (5483S, Cell Signaling Technology, dilution 1:1000),

TBK1 Antibody (3504S, Cell Signaling Technology, dilution 1:1000), Phospho-STING (Ser365) Antibody (72971S, Cell Signaling Technology, dilution 1:1000), STING Antibody (13647S, Cell Signaling Technology, dilution 1:1000), phospho-IRF-3 (Ser396) Antibody (4947S, Cell Signaling Technology, dilution 1:1000), IRF-3 Antibody (4302S, Cell Signaling Technology, dilution 1:1000), phospho-STAT1 (Tyr701) Antibody (9167S, Cell Signaling Technology, dilution 1:1000), STAT1 Antibody (14994S, Cell Signaling Technology, dilution 1:1000), VDAC Antibody (4661S, Cell Signaling Technology, dilution 1:1000), Lamin B1 Antibody (ab16048, Abcam, dilution 1:1000),  $\alpha$ -Tubulin Antibody (3873S, Cell Signaling Technology, dilution 1:1000) and anti- $\beta$ -actin antibody (ab49900, Abcam, dilution 1:1000). The secondary antibodies anti-rabbit IgG-HRP antibody (ab97051, Abcam, dilution 1:20000) and anti-mouse IgG-HRP antibody (ab97023, Abcam, dilution 1:20000) were incubated according to the manufacturer's recommendations. To determine phosphorylated proteins, samples in 1 $\times$  Sample Buffer (191-13272, Fujifilm) were loaded into SuperSep<sup>TM</sup> Phos-tag<sup>TM</sup> gel (199-18011, Fujifilm) and were blotted for BATF2 and IRF3.

To immunoblot native proteins, the cells were lysed in 1 $\times$  NativePAGE<sup>TM</sup> Sample Buffer and 1% Digitonin (BN2008, Thermo Fisher Scientific) and sonicated 15 seconds for 3 times. The BCA protein assays were performed to quantify lysate protein concentrations. The samples were loaded into NativePAGE 4-16%, Bis-Tris, 1.0 mm, Mini Protein Gels (BN1002BOX, Thermo Fisher Scientific) and were run in the NativePAGE Running Buffer (BN2007, Thermo Fisher Scientific). Then, the proteins were transferred to a PVDF membrane in the NuPAGE Transfer Buffer and blotted by a STING Antibody (13647S, Cell Signaling Technology, dilution 1:1000).

HEK-293T and FaDu cells were seeded in 10 cm dishes and were transfected with 1  $\mu$ g/mL FLAG-STING and 1  $\mu$ g/mL BATF2-HA plasmids for 24 hours to assess the interaction

between BATF2 and STING. Experimental cells were lysed on ice by NP40 buffer (50 mM Tris-HCl pH 8.0, 150 mM NaCl, and 0.1% NP-40) supplemented with protease and phosphatase inhibitors. Anti-FLAG M2 Affinity gel (A2220, Millipore Sigma) and anti-HA Agarose (26181, Thermo Fisher Scientific) were used to pull down FLAG-STING and BATF2-HA proteins. The immunoprecipitated proteins were blotted for anti-FLAG M2 Antibody (14793, Cell Signaling Technology, dilution 1:1000) and anti-HA-Tag Antibody (3724, Cell Signaling Technology, dilution 1:1000).

### **Immunofluorescent confocal microscopy**

Cells grown in 4-well chamber culture slides were stained with 100 nM MitoTracker (M7510, Invitrogen) Orange for 15 minutes at 37 °C, followed by fixation in 4% paraformaldehyde/PBS for 15 minutes at room temperature. Fixed cells were permeabilized with 0.1% Triton X-100 for 10 minutes at room temperature. Cells were incubated with primary antibodies anti-HA-488 (2350S Cell Signaling Technology, dilution 1:800) and anti-STING (13647S, Cell Signaling Technology, dilution 1:50) for 1 hour. After washing, cells were incubated with AF647 labeled secondary antibodies for 1 hour followed by staining with Hoechst 33342 (H3570, Life Technologies, dilution 1:5000). Coverslips were mounted in ProLong antifade mountants and imaged with a Nikon A1SI inverted confocal microscope.

### **Subcellular fractionation**

The purification protocol of the nuclei, cytosol and ER membranes by serial centrifugation was adapted from a reported protocol<sup>43</sup>. Briefly, THP-1 STING WT cells were lysed by ~70 iterations of up and down passes of the pestle in a hypotonic buffer. Nuclei were obtained by centrifugation of the lysed cells at 600g for 5 minutes at 4 °C. The nuclear pellet (P600) was resuspended and incubated in the nuclei lysis buffer for 30 minutes on ice and

centrifuged at 10,000g for 30 minutes, and the resulting supernatant was collected as the nuclear fraction. Post-nuclear supernatant (S600) was centrifuged at 5,000g for 10 minutes at 4 °C to remove mitochondrial fraction (P5000) and then centrifuged at 20,000g for 30 minutes at 4 °C to remove lysosomal and plasma membrane fraction (P20000). The supernatant was centrifuged at 100,000g for 1h at 4 °C to obtain the ER fraction (P100000) and the cytosolic fraction (S100000).

### Quantification of gene expression levels

Total RNA was extracted by RNeasy Plus Mini Kit (74136, Qiagen). The RNA concentration was determined using a Nanodrop Spectrophotometer from Thermo Fisher Scientific. Subsequently, the RNA was reverse-transcribed into cDNA using the High-Capacity cDNA Reverse Transcription Kit along with RNase inhibitor (4368814 and N8080119, respectively, Applied Biosystems). The primer sequences have been previously reported<sup>3,4</sup>. Additional primers are as follows: human *BATF2* forward 5'-3' CAGCTGAAGAAGCAGAAGAACCG, reverse 5'-3' TTTTCCAGAGACTCGTGCTGC; mouse *Batf2* forward 5'-3', CACCGCGATCGCATGCAACTCTGTGGGAGTAG, reverse 5'-3' CTAGAAGTGGACTTTGCAGAAG; Mouse *Oas1* forward 5'-3', GCCTGGTCACGCACTGGTA, reverse 5'-3' AAGCCCTGGGCTGTGTTG; mouse *Mx1* forward 5'-3', GGGGAGGAAATAGAGAAAATGAT, reverse 5'-3' GTTTACAAAGGGCTTGCTTGCT; human *CXCL9* forward 5'-3', GTGGTGGTCTTCCCTCTGGG, reverse 5'-3' ACAGCGACCCTTCTCACTAC; human *CXCL10* forward 5'-3', CTCCAGTCTCAGCACCATGA, reverse 5'-3' GCTCCCCTCTGGTTTAAGG; mouse *Ifng* forward 5'-3' TCAAGTGGCATAGATGTGGAAGAA, reverse 5'-3' TGGCTCTGCAGGATTTCATG;

human *ISG54* forward 5'-3', ACGGTATGCTTGGAACGATTG, reverse 5'-3'  
AACCCAGAGTGTGGCTGATG.

### **ELISA and Lumines**

Cells were seeded into six-well or 96-well plates and treated with agonists as indicated. The amount of Ifn- $\beta$  and Tnf- $\alpha$  in the supernatant was measured by a mouse Ifn- $\beta$  kit (luex-mifnbv2, Invivogen) and a Tnf- $\alpha$  ELISA kit (BMS6073, Invitrogen) according to the manufacturer's instructions. A mouse Lumines Discovery Assay kit (LXSAMSM, R&D systems) was also used to quantify cytokines.

### **Tissue histology, immunohistochemistry, and multispectral imaging**

Tongue specimens from mice in the 4-NQO model were fixed in 10% formalin and then serially sectioned before paraffin embedding. The slides were deparaffinized and stained in Mayers Hematoxylin. After washing four times with tap water, the slides were washed with 1× PBS and distilled water. Then, they were stained with Alcoholic-Eosin and dehydrated through ethanol followed by xylene wash.

Human head and neck squamous cell carcinoma specimens were included in tissue microarrays (TMAs). TMAs were stained with anti-BATF2 antibody at 1:200 dilution (ab204510, Abcam). Paired longitudinal specimens from patients who progressed from OPMD to oral cancer were stained for BATF2 using the same protocol. Anti-CD20 antibody (ab64088, Abcam, dilution 1:200) and anti-Tcr  $\gamma$ / $\delta$  antibody (#14-5711-82, ThermoFisher Scientific, dilution 1:100) were used for syngeneic murine tumour specimens. The specimens were incubated with a secondary antibody (PK-4001, Vectastain, dilution 1:100). Immunohistochemical (IHC) staining intensity was quantitated in tumour tissue by selecting a region of interest using Aperio ImageScope or ImageJ, followed by quantification.

For immunofluorescence multispectral imaging, the slides were stained with antibodies against PD-L1 (AF1019, R&D, dilution 1:40), CD206 (24595S, Cell Signaling Technology, dilution 1:400), CD4 (25229S, Cell Signaling Technology, dilution 1:200), T-bet (97135S, Cell Signaling Technology, dilution 1:400), Ly-6G (87048S Cell Signaling Technology, dilution 1:100), and CD8 (98941S, Cell Signaling Technology, dilution 1:200). The slides were then stained with horseradish peroxidase HRP-conjugated secondary antibody and HRP-reactive OPAL fluorescent reagents. The signal was washed off between each staining. Whole-slide scanning was completed using the Vectra Polaris Automated Quantitative Pathology Imaging System by Akoya Biosciences. Regions of Interest (ROIs) were selected by an oral pathologist using the Akoya Phenochart software. ROIs were then scanned at 40 $\times$  resolution.

The subsequent analysis involved employing machine learning algorithms developed within the inForm software package. Assurance of consistent staining intensities across the tissue specimen was established. Tissue regions were classified into distinct categories, namely "stroma," or "other" encompassing elements like empty space. Cellular segmentation encompassed nuclear, cytoplasmic, and membranous domains. We utilized the inForm software package to perform a texture analysis and cell segmentation for the classification of cell phenotypes. Then, we employed the R-language to process the single-cell data set. We first collapsed the metric across multiple ROIs by the sample ID and then conducted a two-sample Wilcoxon test for each marker to compare its mean expression level between groups. We further conducted Akoya's nearest neighbor analysis to reveal the mean cell distance between two phenotypes of interest. For each phenotype pair, we conducted a two-sample Wilcoxon test to compare the mean cell distance between groups. The test result is significant if the p-value is smaller than 0.05.

### **Chromatin immunoprecipitation (ChIP)**

ChIP was performed using the Simple ChIP® Plus Sonication Chromatin IP Kit (56383, Cell Signaling Technology). BMDM were fixed with 1% formaldehyde and then lysed in cell lysis buffer and nuclear lysis buffer. The samples were sonicated at 65% amplitude for 10 minutes before being subjected to pull-down using an anti-H3K27me3 antibody (07-449, Millipore, dilution 1:50) and an anti-H3K4me3 antibody (9751S, Cell Signaling Technology, dilution 1:50). The immunoprecipitated and input DNA was quantified using qPCR. The primers are as follows: mouse *Batf2* promoter forward 5'-ATCACAGCTGCCTCTTCC, reverse 5'-TGCATGTCCCTGGATTGTG; mouse *Ifnb1* promoter forward 5'-TCCCTCAAGGTTCTCTCCTG, reverse 5'-AGCAAAGCCACCAAGAAAGC; mouse *Cxcl9* promoter forward 5'-TTGAAAGGGTGGTTGGC, reverse 5'-3' ATGCCCAATTGCCTCTGG.

### **Oxygen consumption rate assay**

The BMDM were seeded in the seahorse XFp miniplate overnight and then transfected with 3.0 µg/mL ISD for 6 hours. The XFp sensor cartridges were filled with 200 µL pre-warmed XF Calibrant the day before the assay. The cells were treated with 1.5 µM oligomycin, 1.0 µM FCCP, and 0.5µM Rot/AA. The oxygen consumption rate was quantified using a Seahorse XFp Analyzer.

### **Flow Cytometry**

Tumour infiltrating lymphocytes were purified by Ficoll and seeded in complete RPMI with 2-mercaptoethanol (55uM) overnight. Phorbol myristate acetate (PMA) (20ng/ml), ionomycin (1.0 µg/mL) and 1× monensin were added into each well for 4 hours. Cells were collected and stained for viability with Zombie Aqua (423101, BioLegend). Next, cells were incubated with Fc blocker (anti-CD16/32, clone 93, BioLegend, dilution 1:100) for 10 minutes

on ice. The cells were then stained using the following antibodies: anti-CD45 (clone 30-F11, BioLegend, dilution 1:100), anti-CD8 (clone 56-6.7, BioLegend, dilution 1:50), anti-TCR $\beta$  (clone H57-597, BioLegend, dilution 1:40), anti-CD4 (clone RM4-5, BioLegend, dilution 1:40), anti-IFN $\gamma$  (clone XMG1.2, BioLegend, dilution 1:40), anti-p-IRF3 (53539S, Cell Signaling Technology, dilution 1:50), anti-p-TBK1(14590S, Cell Signaling Technology, dilution 1:50), anti-mouse TCR  $\gamma/\delta$  (clone GL3, BioLegend, dilution 1:40), anti-CD3 (clone 17A2, BioLegend, dilution 1:25). Data acquisition and compensation was conducted on flow cytometer and analyzed by FlowJo.

### **Next-generation sequencing and data analyses**

Total RNA from non-treated or treated WT and *Batf2*<sup>-/-</sup> BMDM was processed to bulk sequencing. Samples with an RNA Integrity Number of 8 or greater were subjected to Poly(A) mRNA purification. After the cDNA libraries were validated, the samples were subjected to paired-end 150 bp sequencing on the Illumina NovaSeq S4 platform. Bcl2fastq2 Conversion Software by Illumina was used to de-multiplex Fastq files.

After tumour-infiltrating immune cells were enriched, dead cells in the cell suspension were removed using the EasySep Dead Cell Removal (Annexin V) Kit (17899, STEMCELL Technologies). Following cell preparation, the suspension underwent 10 $\times$  Genomics 3'-single-cell processing and RNA-Seq. The quality of the final libraries was verified using the TapeStation 4200 (Agilent). The final libraries were quantified by Qubit (ThermoFisher). Pooled libraries were subjected to paired-end sequencing on the Illumina NovaSeq platform. Bcl2fastq was used for de-multiplexing Fastq files. Our selection of high-quality transcriptomes was based on the following criteria: (i) qualified cells should exhibit unique feature counts ranging from 200 to 6,000; (ii) mitochondrial reads were limited to fewer than 20%; and (iii) transcriptomes

should demonstrate a unique molecular identifier count of over 500. To mitigate technical artifacts, we controlled the library size effects using the *sctransform* tool and applied the mutual nearest neighbor algorithm to eliminate potential batch effects during integration. In selecting genes for further analysis, we prioritized those exhibiting the highest cell-to-cell variation, totaling 3,008 genes. Additional feature genes were chosen to improve the segregation of the immune subsets as reported<sup>44</sup>.

For whole exome sequencing of NOOC2, genomic DNA was extracted by the Genomic DNA Mini Kit (K182001, Invitrogen). The sequencing data set is deposited to the NCBI SRA with a BioProject ID PRJNA1147735. We only focused on high-quality reads that passed the Illumina RTA filter criteria. The reads were then aligned to the NCBI human reference genome (GRCh37) using BWA<sup>45</sup>. We used Picard to remove the duplicated reads. Putative single-nucleotide variants (SNVs) and small insertions/deletions (Indels) are identified by running four different variant callers, including Strelka, MuSE, VarDict, and Mutect. Then, we filtered out potential false positives and mapping artifacts. To remove germline polymorphisms, we compared the nominated somatic mutations to dbSNP, 1000 Genomes Project, the National Heart, Lung, and Blood Institute's Exome Sequencing Project, and the Genome Aggregation Database (gnomAD). All mutations were annotated by ANNOVAR using the NCBI RefSeq database<sup>46</sup>. The mutational signatures of SNVs were analyzed using SigProfilerSingleSample<sup>47</sup>.

## **Data Availability**

The whole exome sequencing data are deposited in the NCBI SRA with a BioProject accession ID of PRJNA1147735 [<https://www.ncbi.nlm.nih.gov/bioproject/PRJNA1147735>]. The BMDM bulk RNA-Seq data are deposited to the NCBI SRA with a BioProject accession ID of PRJNA1363923 [<https://www.ncbi.nlm.nih.gov/bioproject/PRJNA1363923>]. The single-cell dataset is deposited to

the NCBI SRA with BioProject accession numbers of PRJNA1111664 [<https://www.ncbi.nlm.nih.gov/bioproject/PRJNA1111664>] and PRJNA1298899 [<https://www.ncbi.nlm.nih.gov/bioproject/PRJNA1298899>].

The processed bulk RNA-Seq data from human HNSCC specimens are publicly available through the NCBI Gene Expression Omnibus (GEO) with accession ID GSE310041 [<https://www.ncbi.nlm.nih.gov/geo/query/acc.cgi?acc=GSE310041>]. Raw individual-level sequencing data from human samples are not publicly available due to patient privacy concerns but can be made available upon request after the establishment of a Data Use Agreement and/or a Material Transfer Agreement.

The remaining data are available within the Article, Supplementary Information, or Source Data file. Source data are provided with this paper.

### Code Availability

The code for single-cell RNA-Seq analyses is made available through Github [<https://github.com/yuyingxie/BATF2-IFN>], which is linked to zenodo (DOI: 10.5281/zenodo.17643493).

## References

1. McGrail DJ, *et al.* High tumour mutation burden fails to predict immune checkpoint blockade response across all cancer types. *Annals of oncology : official journal of the European Society for Medical Oncology / ESMO* 32, 661-672 (2021).
2. Cancer Genome Atlas N. Comprehensive genomic characterization of head and neck squamous cell carcinomas. *Nature* 517, 576-582 (2015).
3. Heath BR, *et al.* Saturated fatty acids dampen the immunogenicity of cancer by suppressing STING. *Cell Rep* 42, 112303 (2023).
4. Luo X, *et al.* HPV16 drives cancer immune escape via NLRX1-mediated degradation of STING. *The Journal of clinical investigation* 130, 1635-1652 (2020).
5. Tan YS, *et al.* Mitigating SOX2-potentiated Immune Escape of Head and Neck Squamous Cell Carcinoma with a STING-inducing Nanosatellite Vaccine. *Clin Cancer Res* 24, 4242-4255 (2018).
6. Zhang C, Shang G, Gui X, Zhang X, Bai XC, Chen ZJ. Structural basis of STING binding with and phosphorylation by TBK1. *Nature* 567, 394-398 (2019).
7. Barnett KC, *et al.* An epithelial-immune circuit amplifies inflammasome and IL-6 responses to SARS-CoV-2. *Cell host & microbe* 31, 243-259 e246 (2023).
8. Lo BC, *et al.* Microbiota-dependent activation of CD4(+) T cells induces CTLA-4 blockade-associated colitis via Fc $\gamma$  receptors. *Science (New York, NY* 383, 62-70 (2024).
9. Zhai Z, Lei YL, Wang R, Xie Y. Supervised Capacity Preserving Mapping: A Clustering Guided Visualization Method for scRNAseq data. *Bioinformatics*, (2022).
10. Hao Y, Yan M, Heath BR, Lei YL, Xie Y. Fast and robust deconvolution of tumour infiltrating lymphocyte from expression profiles using least trimmed squares. *PLoS Comput Biol* 15, e1006976 (2019).
11. Li T, *et al.* TIMER2.0 for analysis of tumour-infiltrating immune cells. *Nucleic acids research* 48, W509-W514 (2020).
12. Lei Y, *et al.* The mitochondrial proteins NLRX1 and TUFM form a complex that regulates type I interferon and autophagy. *Immunity* 36, 933-946 (2012).
13. Ishikawa H, Barber GN. STING is an endoplasmic reticulum adaptor that facilitates innate immune signalling. *Nature* 455, 674-678 (2008).

14. Seth RB, Sun L, Ea CK, Chen ZJ. Identification and characterization of MAVS, a mitochondrial antiviral signaling protein that activates NF-kappaB and IRF 3. *Cell* 122, 669-682 (2005).
15. Shang G, Zhang C, Chen ZJ, Bai XC, Zhang X. Cryo-EM structures of STING reveal its mechanism of activation by cyclic GMP-AMP. *Nature* 567, 389-393 (2019).
16. Oh MH, *et al.* Targeting glutamine metabolism enhances tumour-specific immunity by modulating suppressive myeloid cells. *The Journal of clinical investigation* 130, 3865-3884 (2020).
17. Liu PS, *et al.* alpha-ketoglutarate orchestrates macrophage activation through metabolic and epigenetic reprogramming. *Nature immunology* 18, 985-994 (2017).
18. Reinfeld BI, *et al.* Cell-programmed nutrient partitioning in the tumour microenvironment. *Nature* 593, 282-288 (2021).
19. Sun X, *et al.* Amplifying STING activation by cyclic dinucleotide-manganese particles for local and systemic cancer metalloimmunotherapy. *Nat Nanotechnol* 16, 1260-1270 (2021).
20. Gajewski TF, Higgs EF. Immunotherapy with a sting. *Science (New York, NY* 369, 921-922 (2020).
21. Li W, *et al.* cGAS-STING-mediated DNA sensing maintains CD8(+) T cell stemness and promotes antitumour T cell therapy. *Sci Transl Med* 12, (2020).
22. Wang Z, *et al.* Syngeneic animal models of tobacco-associated oral cancer reveal the activity of in situ anti-CTLA-4. *Nat Commun* 10, 5546 (2019).
23. Yang CY, *et al.* The transcriptional regulators Id2 and Id3 control the formation of distinct memory CD8+ T cell subsets. *Nature immunology* 12, 1221-1229 (2011).
24. Vitale-Cross L, *et al.* Metformin prevents the development of oral squamous cell carcinomas from carcinogen-induced premalignant lesions. *Cancer Prev Res (Phila)* 5, 562-573 (2012).
25. Baird JR, *et al.* Evaluation of Explant Responses to STING Ligands: Personalized Immunosurgical Therapy for Head and Neck Squamous Cell Carcinoma. *Cancer research* 78, 6308-6319 (2018).
26. Barber GN. STING: infection, inflammation and cancer. *Nature reviews* 15, 760-770 (2015).

27. Cheng N, *et al.* A nanoparticle-incorporated STING activator enhances antitumour immunity in PD-L1-insensitive models of triple-negative breast cancer. *JCI Insight* 3, (2018).

28. Corrales L, *et al.* Direct Activation of STING in the Tumour Microenvironment Leads to Potent and Systemic Tumour Regression and Immunity. *Cell Rep* 11, 1018-1030 (2015).

29. Fu J, *et al.* STING agonist formulated cancer vaccines can cure established tumours resistant to PD-1 blockade. *Sci Transl Med* 7, 283ra252 (2015).

30. Leach DG, *et al.* STINGel: Controlled release of a cyclic dinucleotide for enhanced cancer immunotherapy. *Biomaterials* 163, 67-75 (2018).

31. Luo M, *et al.* A STING-activating nanovaccine for cancer immunotherapy. *Nat Nanotechnol* 12, 648-654 (2017).

32. Meric-Bernstam F, *et al.* Phase I Dose-Escalation Trial of MIW815 (ADU-S100), an Intratumoural STING Agonist, in Patients with Advanced/Metastatic Solid Tumours or Lymphomas. *Clin Cancer Res* 28, 677-688 (2022).

33. Mukai K, *et al.* Activation of STING requires palmitoylation at the Golgi. *Nat Commun* 7, 11932 (2016).

34. Taner HF, *et al.* SOX2-induced IL1alpha-mediated immune suppression drives epithelial dysplasia malignant transformation. *bioRxiv*, (2024).

35. Leone RD, *et al.* Glutamine blockade induces divergent metabolic programs to overcome tumour immune evasion. *Science (New York, NY* 366, 1013-1021 (2019).

36. Satoh T, *et al.* The Jmjd3-Irf4 axis regulates M2 macrophage polarization and host responses against helminth infection. *Nature immunology* 11, 936-944 (2010).

37. Zhu D, *et al.* EZH2 inhibition and 5-azacytidine enhance antitumour immunity in PTEN-deficient glioblastoma by activation viral mimicry response. *J Immunother Cancer* 13, (2025).

38. Fang L, *et al.* Methionine restriction promotes cGAS activation and chromatin untethering through demethylation to enhance antitumour immunity. *Cancer cell* 41, 1118-1133 e1112 (2023).

39. Cao L, *et al.* BATF2 inhibits the stem cell-like properties and chemoresistance of gastric cancer cells through PTEN/AKT/beta-catenin pathway. *Theranostics* 14, 7007-7022 (2024).

40. Liu J, Li J, Tuo Z, Hu W, Liu J. BATF2 inhibits PD-L1 expression and regulates CD8+ T-cell infiltration in non-small cell lung cancer. *The Journal of biological chemistry* 299, 105302 (2023).
41. Zhang X, *et al.* BATF2 prevents glioblastoma multiforme progression by inhibiting recruitment of myeloid-derived suppressor cells. *Oncogene* 40, 1516-1530 (2021).
42. Bian Y, *et al.* Cancer SLC43A2 alters T cell methionine metabolism and histone methylation. *Nature* 585, 277-282 (2020).
43. Wieckowski MR, Giorgi C, Lebiedzinska M, Duszynski J, Pinton P. Isolation of mitochondria-associated membranes and mitochondria from animal tissues and cells. *Nat Protoc* 4, 1582-1590 (2009).
44. Gong W, *et al.* Cancer-specific type-I interferon receptor signaling promotes cancer stemness and effector CD8+ T-cell exhaustion. *Oncoimmunology* 10, 1997385 (2021).
45. Li H, Durbin R. Fast and accurate short read alignment with Burrows-Wheeler transform. *Bioinformatics* 25, 1754-1760 (2009).
46. Wang K, Li M, Hakonarson H. ANNOVAR: functional annotation of genetic variants from high-throughput sequencing data. *Nucleic Acids Res* 38, e164 (2010).
47. Petljak M, *et al.* Characterizing Mutational Signatures in Human Cancer Cell Lines Reveals Episodic APOBEC Mutagenesis. *Cell* 176, 1282-1294 e1220 (2019).

## Acknowledgments

The FLAG-STING expression plasmid is kindly provided by Dr. Glen N. Barber at the University of Miami. We sincerely thank Dr. Gabriel Nuñez at the University of Michigan for providing the *Tcrd*<sup>-/-</sup> mice. This project was funded by NIH grants R03DE027399 (YLL), R01 DE026728 (YLL), R01 DE030691 (JJM), R01 DE031951 (JJM), U01 DE033330 (YLL), and U01 DE029255 (YLL). Q.H. and L.W. were supported by U24 CA274159. The core facilities are supported, in part, by P30 CA016672.

## Author Contributions Statement

W.G., H.F.T., Y.W., Y.H., X.Z., Z.L., X.H., C.U., K.C.D., K.O., C.R.D., F.N., M.Z., W.C., Z.R.F., L.B., J.L., and Y.Y. performed experiments and contributed to data acquisition. W.G. and Y.L.L. designed the project with significant intellectual input from J.J.M., S.D., A.G.S., and D.N., Y.W., C.D.P., E.B., and Y.X. advised on statistical analysis and performed data analyses. Y.W., A.Y., Z.Z., Y.X., and Y.L.L. performed single-cell analyses and biostatistical analyses. Q.H., and L.W. performed analyses for the NOOC2 whole-exome sequencing and mutation profile data set. G.T.W. and S.B.C. provided completely de-identified discarded/archived human material. H.W. and S.A. provided key resources and technical support. M.Z. and J.N.M. provided key cell lines. W.G., H.F.T., Y.H., Y.X., and Y.L.L. wrote the manuscript, and all authors edited the manuscript and have read and agreed to its contents. Y.L.L. and J.J.M. supervised the study.

## Competing Interests Statement

Y.L.L. and J.J.M. are co-founders and serve on the advisory board of Saros Therapeutics Inc. Y.L.L. licensed NOOC1 cells to Kerafast Inc and Applied Biological Materials Inc. The other authors do not have competing interests relevant to this study for disclosure.

ARTICLE IN PRESS

**Figure Legends**

**Figure. 1:** BATF2 strongly correlates with IFN-I and Th1 signatures in the TME of human HNSCC. **a**, A supCPM rendering of 38,862 transcriptomes from HPV<sup>-</sup> HNSCC and 20,703 transcriptomes from HPV<sup>+</sup> HNSCC is shown. The significantly altered clusters between the two groups are highlighted in red. **b**, Scatter plots for the correlation between the expression levels of *BATF2* and those of *IFNB1*, *MX1*, and *ISG54* in  $n = 520$  HNSCC specimens from the TCGA database are shown. **c**, The correlation between the expression levels of *BATF2* and TIL subsets deconvolved by FARDEEP in HNSCC specimens ( $n = 520$ ) from the TCGA database is shown. **d-e**, After filtering out suboptimal cores, cores from 200 patients with HNSCC were included for BATF2 staining scoring. Correlations between HNSCC-specific/TME-specific BATF2 and CD8 staining scores are shown. **f-g**, Paired specimens from five patients who progressed from OPMD to oral squamous cell carcinoma were stained for BATF2, whose staining was quantified using ImageJ ( $n = 22$  ROI for OPMD,  $n = 24$  ROI for HNSCC; data are presented as mean  $\pm$  SEM; unpaired two-tailed t-test). **h-i**, A portion of each human oral squamous cell carcinoma specimen was used to prepare TMA for BATF2 staining, while the remaining tissue was injected with CDA for qPCR quantification of the *IFNB1/PTPRC* ratio ( $n = 8$ ). Spearman correlation analysis was performed to evaluate the relationship between BATF2 staining scores and the *IFNB1/PTPRC* ratio. The shaded area represents the 95% confidence interval. Data in b, c, e, and i were analyzed using Spearman's correlation test (\*\*\*\*P < 0.0001). Scale bars in d, f and h represent 100  $\mu$ m. Source data are provided as a Source Data file.

**Figure. 2:** BATF2 is indispensable for cytoplasmic DNA-mediated IFN-I response in macrophages. **a**, We confirmed the establishment of *Batf2*-targeted deletion in mice (left panel). The mRNA levels of *Batf2* in BMDM from indicated genotypes are shown (right panel,  $n = 3$

biologically independent samples; data are presented as mean  $\pm$  SEM; unpaired two-tailed t-test).

**b**, BMDM were transfected with 2.0  $\mu$ g/mL ISD and 1.0  $\mu$ g/mL poly(I:C) for 8 hours, and total mRNA was extracted for bulk RNA sequencing. The transcriptomes were compared between wildtype and *Batf2*<sup>-/-</sup> BMDM. Data represent biologically independent samples ( $n = 2$  per group).

**c**, GSEA shows the significantly altered pathways between wildtype and *Batf2*<sup>-/-</sup> BMDM in response to STING stimulation. **d-g**, BMDM from wildtype and *Batf2*<sup>-/-</sup> mice were transfected with 3.0  $\mu$ g/mL ISD (d), 1.0  $\mu$ g/mL cGAMP (e), 1.0  $\mu$ g/mL poly(I:C) (f) or 1.0  $\mu$ g/mL 5'ppp-dsRNA (g) for 16 hours. Total mRNA was extracted for qPCR. The fold changes of *Ifnb1*, pan-

*Ifna*, and *Cxcl10* are shown as indicated. Data represent biologically independent experiments ( $n = 3$ ). **h-i**, Wild-type and *Batf2*<sup>-/-</sup> BMDM were transfected with 3.0  $\mu$ g/mL ISD (h) or 1.0  $\mu$ g/mL cGAMP (i) for 24 hours. The concentration of Ifn- $\beta$  in the supernatant was measured by

ELISA. Data represent biologically independent experiments ( $n = 3$ ). **j**, Wild-type and *Batf2*<sup>-/-</sup> BMDM were incubated with 10.0  $\mu$ g/mL diABZI for 8 hours. Ifn- $\beta$  in the supernatant was measured by ELISA. Data represent biologically independent experiments ( $n = 3$ ). **k-l**, Wild-type and *Batf2*<sup>-/-</sup> BMDM were transfected with 1.0  $\mu$ g/mL poly(I:C) (k) or 1.0  $\mu$ g/mL 5'ppp-dsRNA (l) for 24 hours. Ifn- $\beta$  in the supernatant was quantified by ELISA. Data represent biologically independent experiments ( $n = 3$ ). **m-n**, Wild-type and *Batf2*<sup>-/-</sup> BMDM were transfected with 3.0  $\mu$ g/mL ISD (m) or 1.0  $\mu$ g/mL cGAMP (n). Cell lysates were collected at the indicated time

points for immunoblot analysis. The experiment was performed in two biologically independent experiments. Comparisons in d-l were made using two-way ANOVA followed by multi-comparison tests and data are presented as mean  $\pm$  SEM. Source data are provided as a Source Data file.

**Figure. 3:** BATF2 promotes the STING-IFN-I pathway in HNSCC cells. **a-b**, FaDu and UMSCC22A cells were transduced with empty vector (EV) or pMXs-BATF2-2HA retrovirus to generate stable BATF2 overexpression HNSCC cell lines. The cells were transfected with 1.0  $\mu$ g/mL STING plasmid for 16 hours. Total mRNA was collected for qPCR quantification of IFN-I signature genes. Data represent biologically independent experiments ( $n = 3$ ). **c-d**, UMSCC108 and UMSCC49 cells were transduced with EV or CRISPR-Cas9 lentiviruses and then selected using 10  $\mu$ g/mL puromycin to obtain stable cell lines. The EV control and *BATF2*<sup>-/-</sup> cells were transfected with 1.0  $\mu$ g/mL STING plasmid for 16 hours. Total mRNA was collected for qPCR quantification of IFN-I signature genes. Data represent biologically independent experiments ( $n = 3$ ). **e**, EV and BATF2-expressing FaDu and UMSCC22A cells were transfected with 1.0  $\mu$ g/mL STING plasmid for 24 hours. The protein lysates were subjected to SDS-PAGE and immunoblotting of the indicated markers. Data represent biologically independent experiments ( $n = 2$ ). **f**, EV and *BATF2*<sup>-/-</sup> UMSCC108 and UMSCC49 cells were transfected with 1.0  $\mu$ g/mL STING plasmid for 24 hours. The protein lysates were subjected to SDS-PAGE and immunoblotting of the indicated markers. Data represent biologically independent experiments ( $n = 2$ ). Comparisons in a-d were made using two-way ANOVA followed by multi-comparison tests and data are presented as mean  $\pm$  SEM. Source data are provided as a Source Data file.

**Figure. 4:** BATF2 interacts with STING in the ER and promotes STING oligomerization. **a**, Human HNSCC ( $n = 2$ ) FFPE slides were stained with an antibody against BATF2. **b**, THP-1 cells were incubated with 10  $\mu$ g/mL cGAMP mixed with human albumin at 1:1 ratio overnight. The nuclei, cytosol, and ER-associated membrane components were obtained by sucrose gradient centrifugation. Immunoblotting was performed for proteins as shown. **c**, UMSCC22A-

BATF2 cells were transfected with 0.08 µg/well FLAG-STING plasmids and 0.35 µg/well cGAMP for 16 hours. The staining pattern of STING, BATF2, and mitochondria was evaluated using confocal microscopy (scale bar: 5.0 µm). **d-g**, HEK-293T and FaDu cells were co-transfected with 1.0 µg/mL BATF2-HA and 1.0 µg/mL FLAG-STING plasmids for 24 hours. Reciprocal co-immunoprecipitation of BATF2 and STING was performed. **h**, co-IP was performed to verify the interaction between Sting and Batf2 in RAW246.7 cells. **i**, HEK-293T cells were transfected with 1.0 µg/mL BATF2-HA and 1.0 µg/mL FLAG-tagged STING truncation mutant plasmids for 24 hours. Co-IP was performed to examine the interaction between BATF2 and STING truncation mutants. **j**, Wild-type and *Batf2*<sup>-/-</sup> BMDM were transfected with 3.0 µg/mL ISD for 0, 2, 4, and 8 hours. Protein lysates were resolved using native PAGE and then immunoblotted to assess the oligomerization of STING. **k**, A cartoon shows the domain structure of BATF2. The phosphorylation sites were predicted using PhosphoSitePlus. **l**, THP-1 cells were incubated with 10 µg/mL cGAMP admixed with human albumin overnight. Protein lysates from the control and treated groups were resolved using phospho-tag gel electrophoresis and immunoblotted to assess the phosphorylation of BATF2 and IRF3. The protein samples from the same experiment were also subjected to SDS-PAGE as another control. **m**, *Batf2*<sup>-/-</sup> bone marrow cells were transduced with full-length or 179A or 227A BATF2 mutant retroviruses and differentiated into BMDM, which were then transfected with 2.0 µg/mL ISD for 8 hours. The protein lysates were subjected to SDS-PAGE and immunoblotted against the indicated markers. The experiments in b-c, h-j, and l were performed in two biologically independent experiments. The experiments in d-g and m were performed in three biologically independent experiments.

**Figure. 5:** Glutamine metabolism epigenetically silences BATF2 and remodels oxidative phosphorylation to dampen the STING-IFN-I response. **a-b**, BMDM were cultured in media containing glutamine (0 g/L, 0.5 g/L, or 5.0 g/L) for 24 hours, followed by transfection with STING agonists. **c-d**, BMDM were cultured in media containing 0.5 g/L (c) or 5 g/L (d) glutamine and transfected with cGAMP with or without of BPTES. Data are compared using one-way ANOVA. **e-f**, Ifn- $\beta$  in the supernatant from Fig. 5a-b was quantified by ELISA. **g**, BMDM were cultured in media containing varied levels of glutamine and then transfected with cGAMP. The protein lysates were subjected to immunoblotting. Data represent two biologically independent experiments. **h**, BMDM were cultured in media containing varied levels of glutamine and transfected with ISD. ChIP analysis of the H3K27me3 mark in the promoter regions of *Batf2* is compared using one-way ANOVA. **i**, BMDM were cultured in media containing 0 g/L or 5.0 g/L glutamine for 24 hours and transfected with ISD and OCR was compared. **j**, Wild-type and *Batf2*<sup>-/-</sup> BMDM were transfected with ISD and OCR was compared. **k**, Female C57BL6/J mice on a control diet or glutamine-rich diet were implanted with NOOC1 cells subcutaneously. Mice were treated with PBS or c-di-AMP intratumoural injection ( $n = 8$ ). **l-m**, The combination of CDA and JHU-083 was administered for 2 weeks ( $n = 8$ ). **n**, UMAP rendering of scRNA-Seq of the TILs separated from 5k ( $n = 8$  mice per group) shown above is generated. **o**, The relative cluster size change percent is shown. **p**, The *Batf2* expression level in each cluster is shown. **q**, The expression levels of *Batf2* were compared using a Wilcoxon test. **r**, Bulk RNA-Seq was performed for 15 HNSCC specimens. A correlation analysis between BATF2-IFN-I target genes and glutamine metabolism is shown. Data in Fig. 5a-h represent biologically independent experiments ( $n = 3$ , mean  $\pm$  SEM). Data in Fig. 5i-j were compared by an unpaired two-tailed t-test and represent biologically independent samples ( $n = 3$ ,

mean  $\pm$  SEM). Comparisons in a-b and e-f were made using two-way ANOVA, followed by multi-comparison tests. The tumour growth in Fig. 5k-m was compared using the generalized estimating equation (GEE) model.

**Figure. 6:** HNSCC-specific BATF2 promotes spontaneous IFN-I- and  $\gamma\delta$  T-cell-dependent tumour rejection. **a**, Stable EV control and Batf2-expressing MOC2-E6/E7 cells were transfected with Sting plasmid for 16 hours. The mRNA was quantified by qPCR ( $n = 3$ ). **b-c**, EV control and Batf2-expressing MOC2-E6/E7 cells were transfected with Sting plasmid for 24 hours. **b**, The amount of Ifn- $\beta$  in the supernatant was measured by ELISA ( $n = 3$ ). **c**, protein lysates were harvested for immunoblotting against the indicated markers. **d**, EV or Batf2-expressing MOC2-E6/E7 cells were implanted subcutaneously and monitored for tumour burden in the wild-type female C57BL6/J mice ( $n = 5$  each group). The tumour growth was compared using the GEE model. **e**, EV or Batf2-expressing MOC2-E6/E7 cells were implanted in *Ifnar1*<sup>-/-</sup> mice ( $n = 9$  in EV group;  $n = 10$  in Batf2-MOC2-E6/E7 group). Tumour growth was compared using the GEE model. **f-i**, One million the EV or Batf2-expressing MOC2-E6/E7 cells were implanted subcutaneously in wild-type mice. On days 7, 14, and 21 after implantation, tumour tissues were processed into single-cell suspensions. Flow cytometry was used to evaluate the presence of p-Tbk1 $^+$ , p-Irf3 $^+$ , CD8 $^+$ , and TCR $\gamma\delta$  $^+$  cells in the TME ( $n = 4$  in the Day 7 Batf2 and the Day 14 EV groups;  $n = 5$  for other groups). **j**, UMAP rendering of single-cell immune profiling of the TILs separated from the control ( $n = 5$ ) and Batf2-expressing ( $n = 5$ ) tumours grown in wild-type C57BL6/J mice from Fig. 6d is shown. The significantly altered clusters between the two groups are labeled in red. **k**, The relative percentage of TILs is shown. **l**, T-cell clusters (13+16) were separated, and the volcano plot shows the differentially expressed genes between groups. **m**, A

gene set enrichment analysis was performed to identify the most significantly altered pathways in T-cells from Fig. 6d. Comparisons in a-b were made using two-way ANOVA followed by multi-comparison tests. Comparisons in f-i were made using an unpaired two-way t-test. Data in a-b and d-i are presented as mean  $\pm$  SEM. Source data are provided.

**Figure. 7:** *Batf2* deficiency in the host expedited the initiation of tumours. **a**, One million MOC2-E6/E7 cells were implanted into female littermate control wild-type ( $n = 8$ ) and *Batf2*<sup>-/-</sup> ( $n = 7$ ) mice subcutaneously. **b**, TILs were enriched by Ficoll-Paque gradient centrifugation and subjected to multispectral flow cytometric analysis ( $n = 5$  for the p-Irf3<sup>+</sup> panel;  $n = 8$  for other panels). **c**, Three million NOOC2 cells were implanted into female littermate control wild-type ( $n = 5$ ) and *Batf2*<sup>-/-</sup> ( $n = 6$ ) mice subcutaneously. **d**, p-Irf3<sup>+</sup> cells ( $n = 4$  in the control group;  $n = 7$  in the *Batf2*<sup>-/-</sup> group), CD4<sup>+</sup> and CD8<sup>+</sup> T-cells ( $n = 6$  in the control group;  $n = 4$  in the *Batf2*<sup>-/-</sup> group) in the TME were quantified by flow cytometry. **e**, One million 4MOSC1 cells in 40  $\mu$ L PBS were injected into the tongues of female wild-type and *Batf2*<sup>-/-</sup> mice ( $n = 4$ ). Tumour growth between groups shown in Fig. 7a, 7c, and 7e was compared using the GEE model. Comparisons in b and d were made using an unpaired two-tailed t-test. Data in a-e are presented as mean  $\pm$  SEM. **f-g**, Using a 4-NQO model, lesion-free survival was compared between wild-type ( $n = 17$ , 9 male and 8 female) and *Batf2*<sup>-/-</sup> ( $n = 16$ , 9 male and 7 female) mice using a Log-rank test (f). The characteristics of disease burden in the oral cavity were compared using the GEE model (g). **h-i**, Multispectral imaging analysis was compared after HNSCC histology was verified. Cell phenotypes were established utilizing image features obtained from texture analysis and cell segmentation. The count of CD206<sup>+</sup> myeloid cells (h) and the expression levels of nuclear Tbet among CD8<sup>+</sup>Tbet<sup>+</sup> T-cells (i) were compared using a Wilcoxon rank sum test

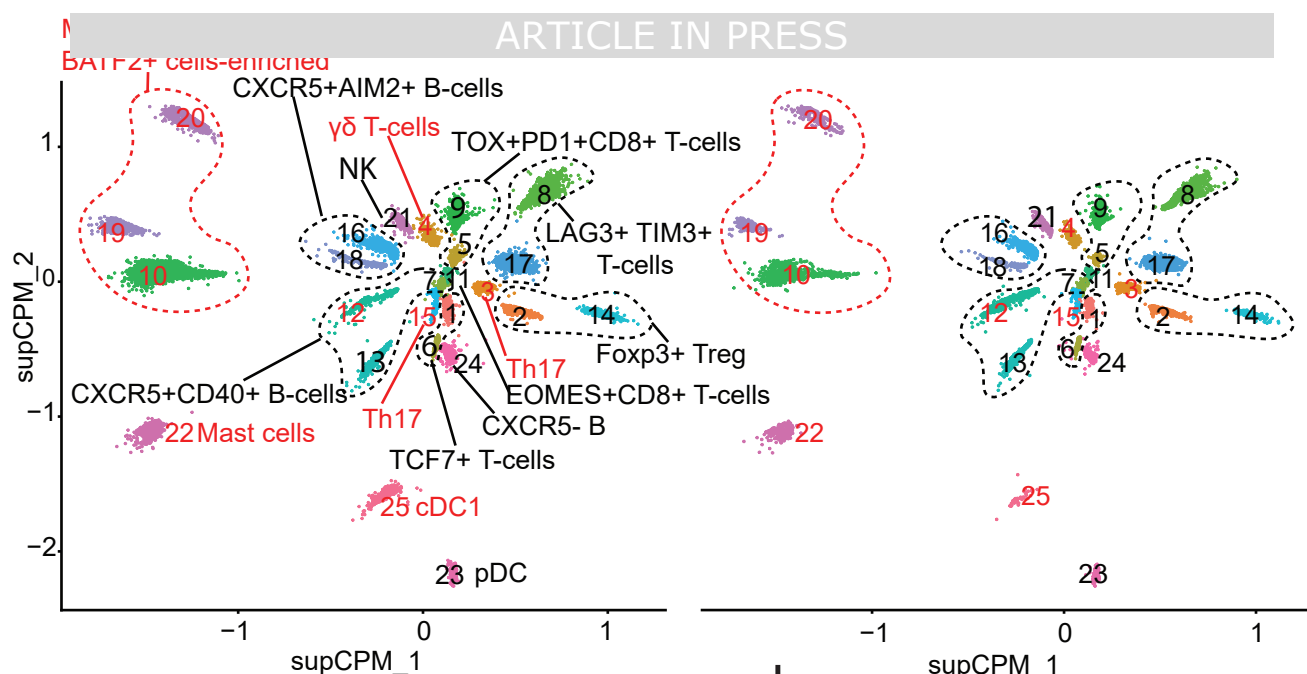
with continuity correction. The comparison was based on whole-slide analyses of 10 tongue specimens ( $n = 5$  per genotype). The box plots show the median (center line), 25th and 75th percentiles (bounds of the box). The whisker extends to 1.5 interquartile ranges. Scale bars represent 100  $\mu\text{m}$ . Source data are provided as a Source Data file.

### Editorial summary

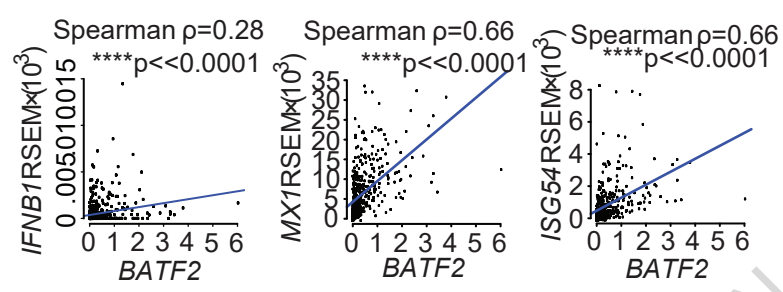
STING-type-I interferon pathway regulates the immunogenicity of several cancer types, including head and neck squamous cell carcinoma. Here the authors describe that glutamine metabolism in the tumour microenvironment dampens the STING-type-I interferon pathway by epigenetically silencing the expression of BATF2, which functions as a tumour suppressor.

**Peer Review Information:** *Nature Communications* thanks Robert Saddawi-Konefka, Walter Storkus and the other anonymous, reviewer(s) for their contribution to the peer review of this work. A peer review file is available.

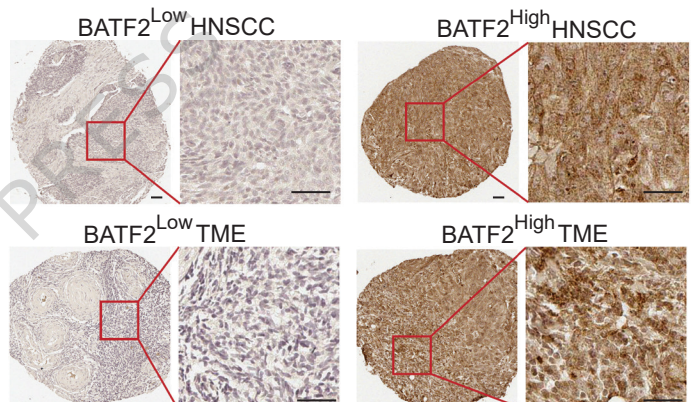
a



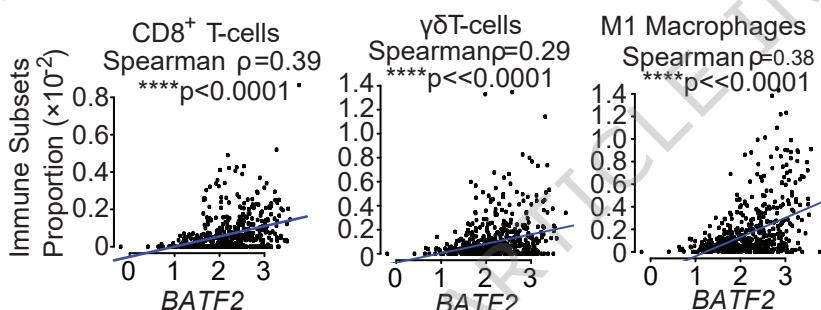
b



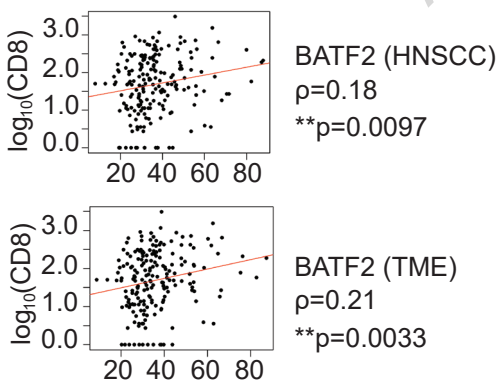
d



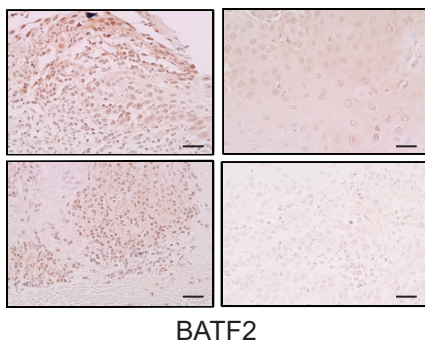
c



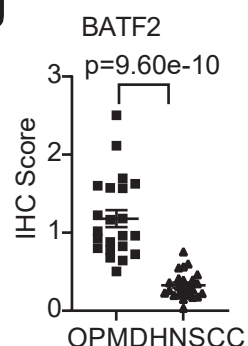
e



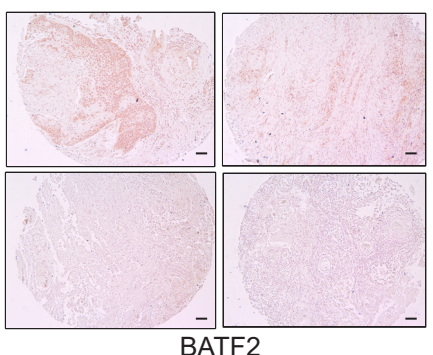
f



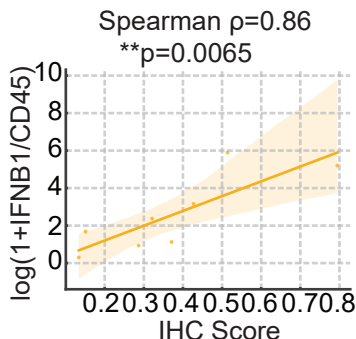
g

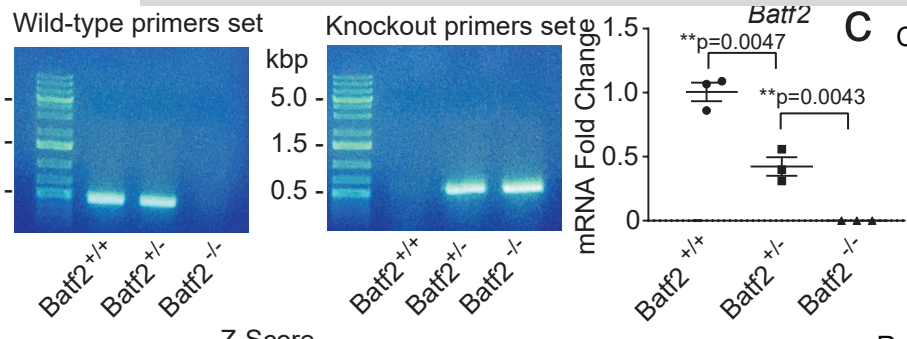
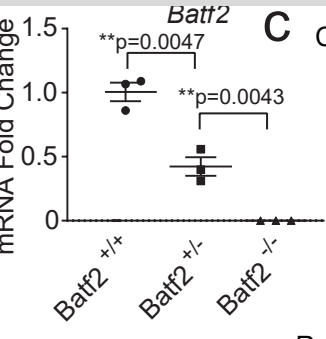
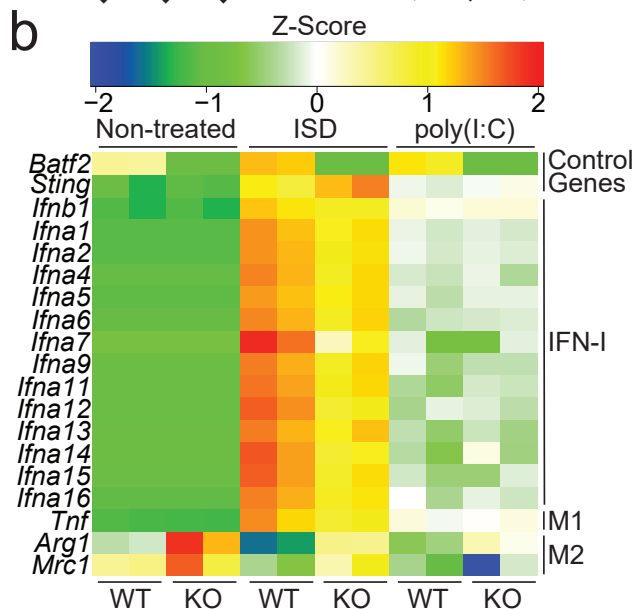
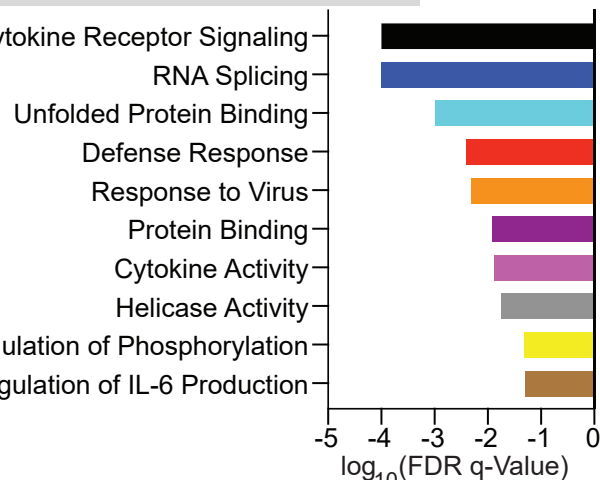
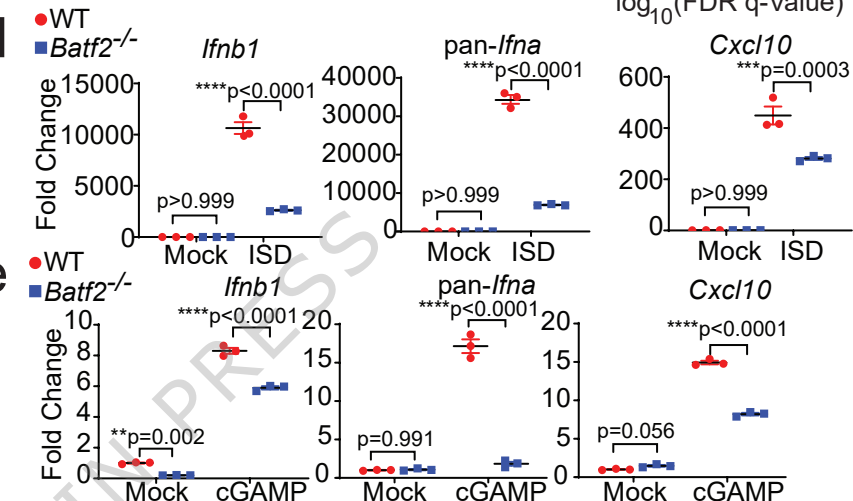
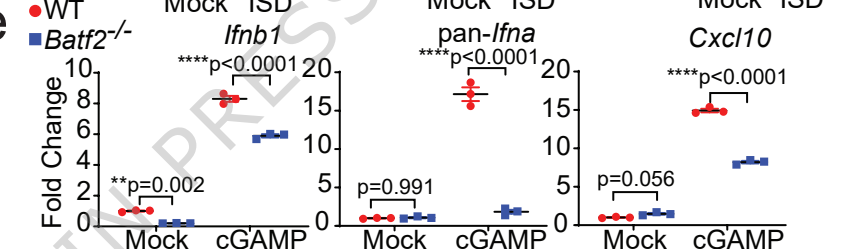
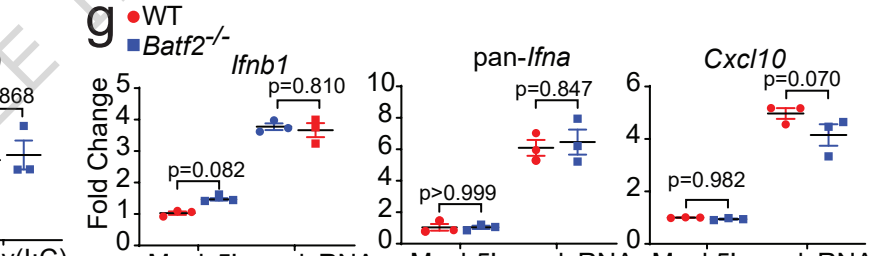
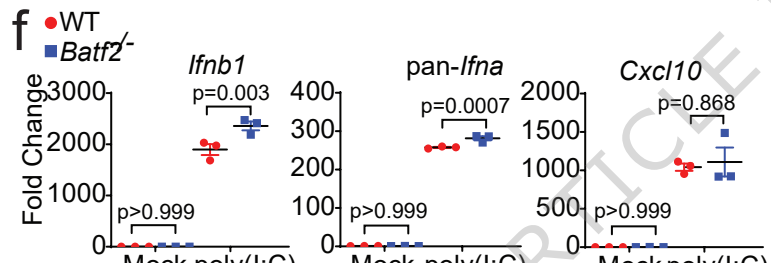
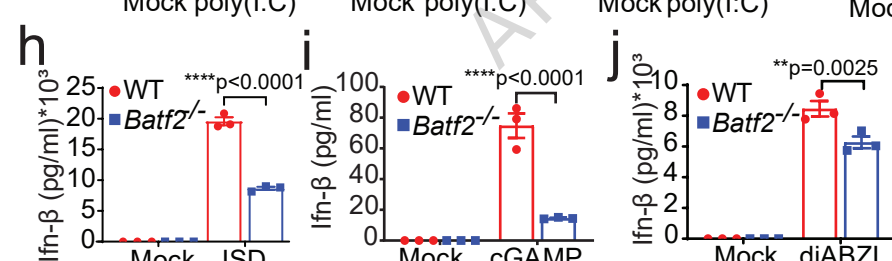
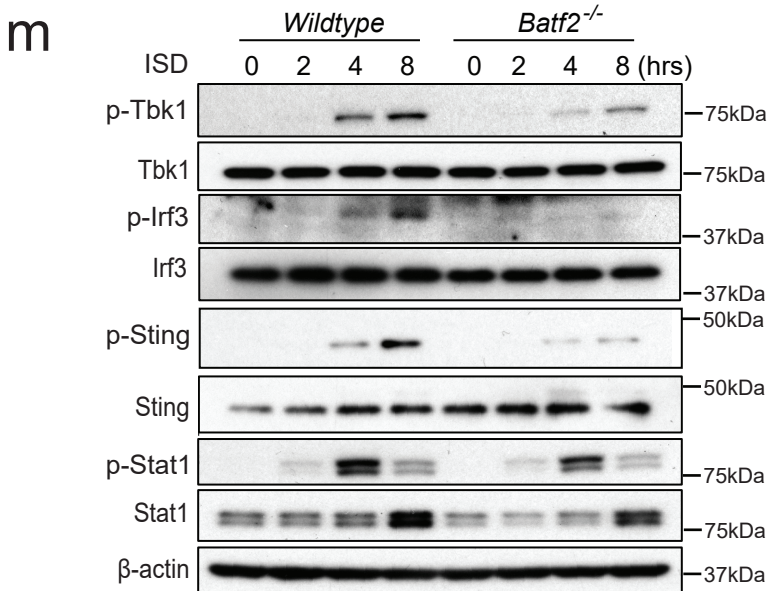
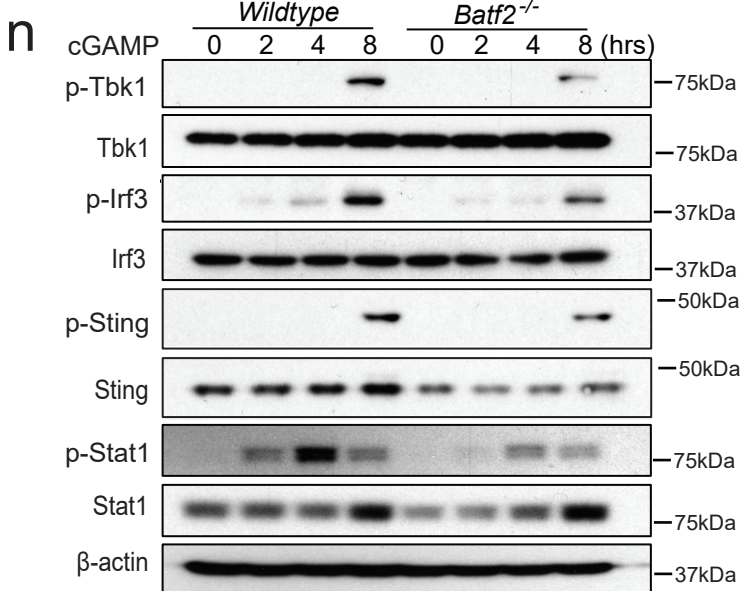


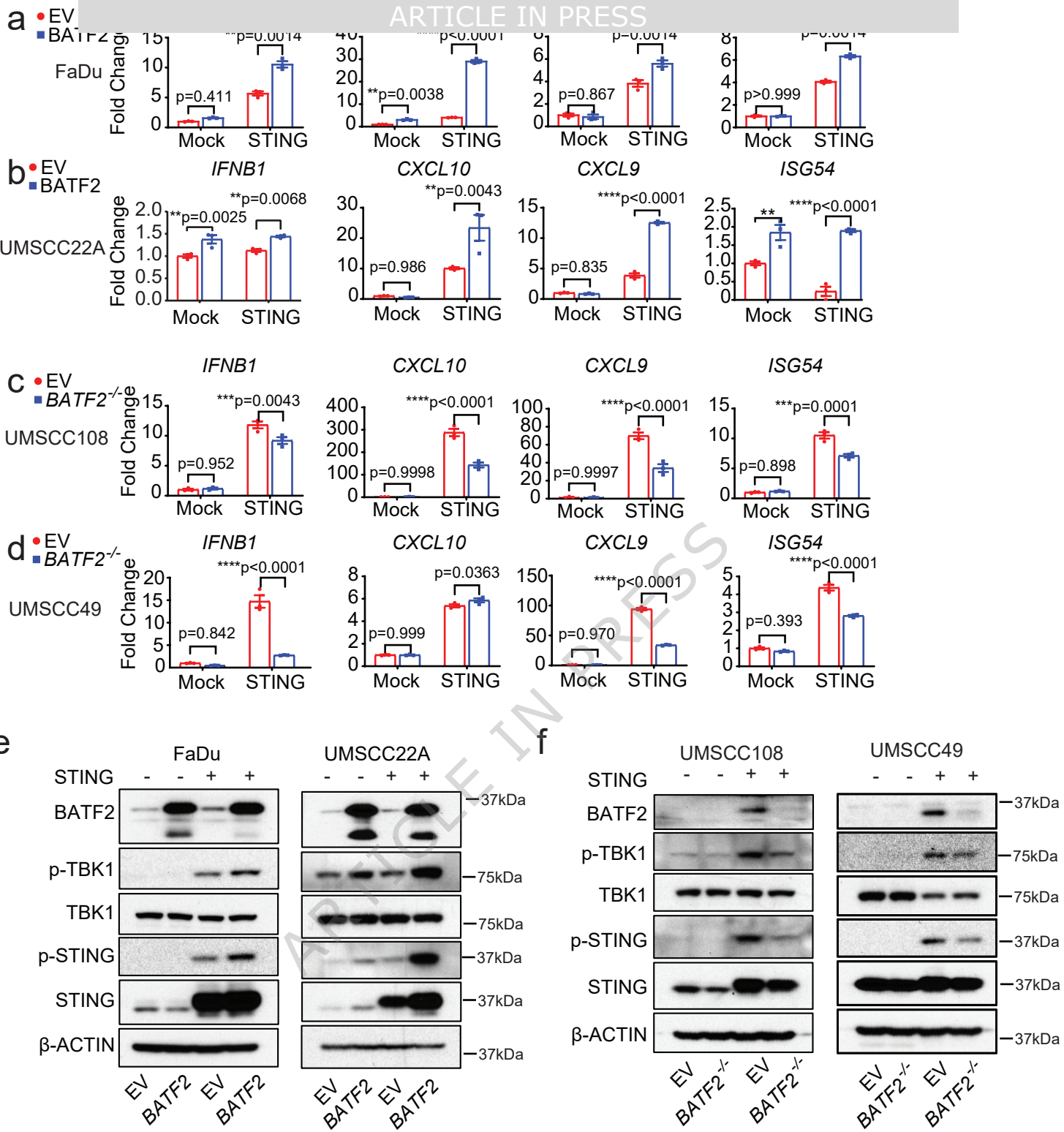
h

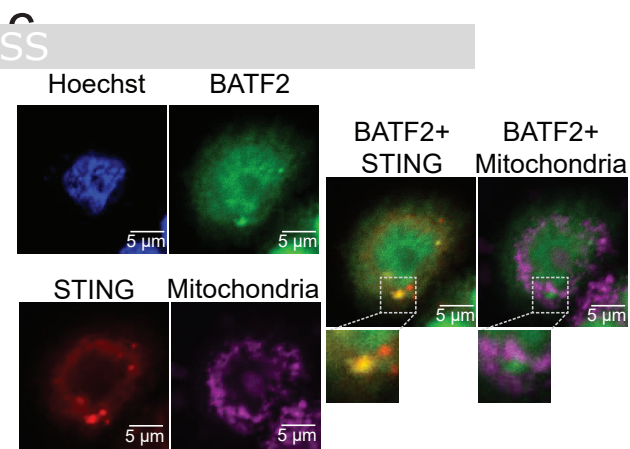
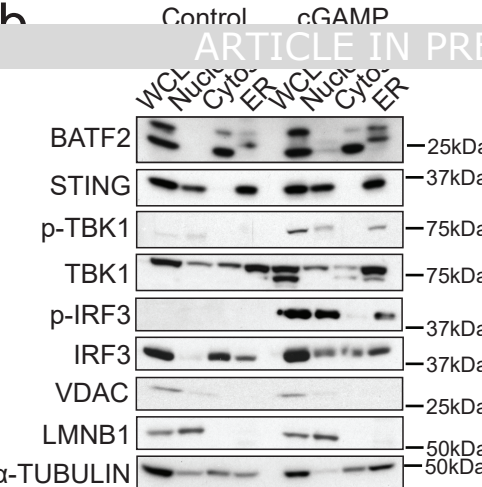
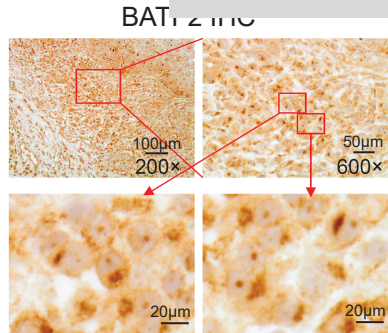
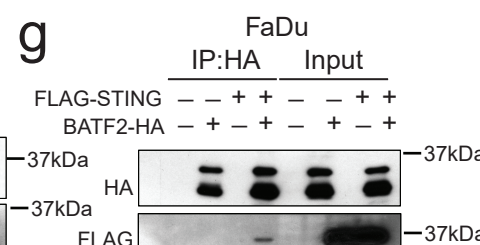
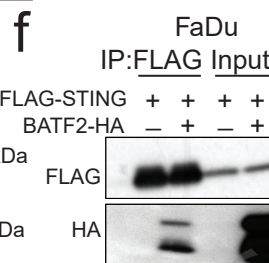
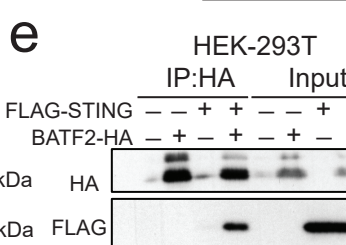
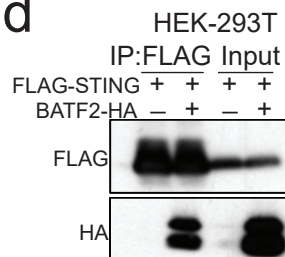
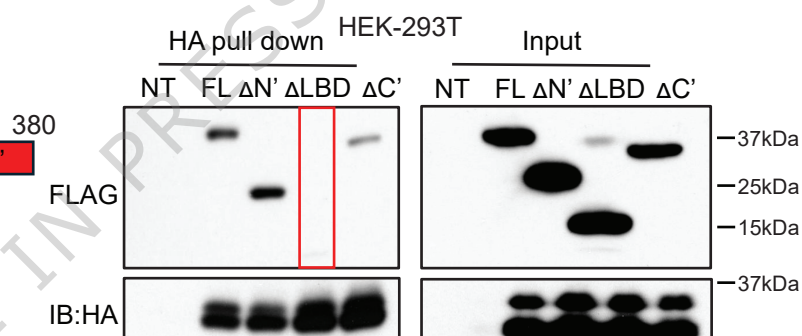
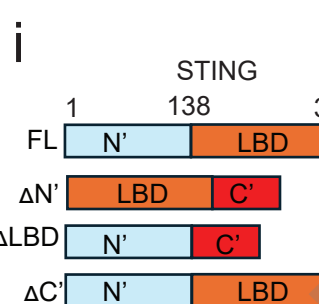
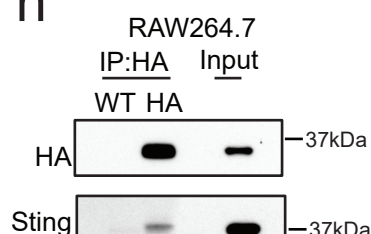
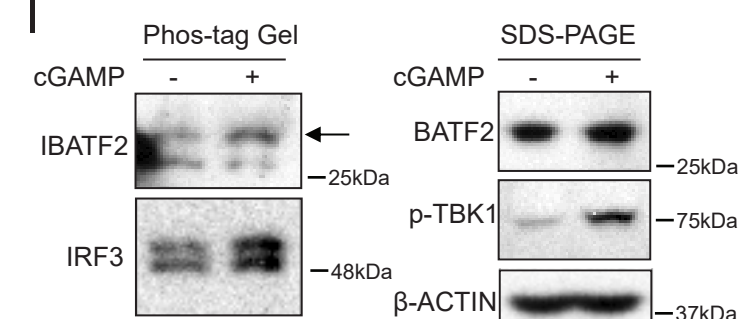
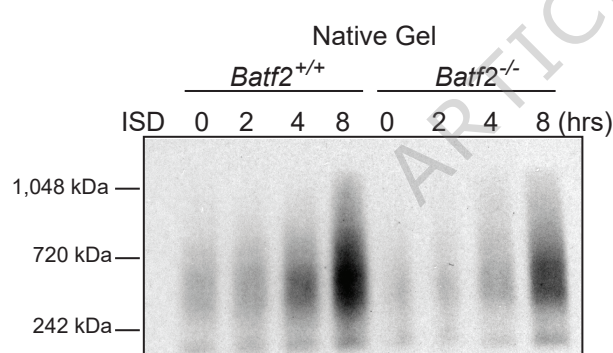
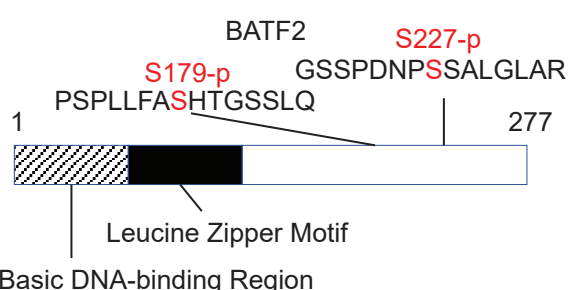


i



**a****b****c****d****e****g****f****h****m****n**



**a****d****h****j****k****m**